Application of the shipborne remote sensing supersite OCEANET for profiling of Arctic aerosols and clouds during Polarstern cruise PS106

Hannes J. Griesche, Patric Seifert, Albert Ansmann, Holger Baars, Carola Barrientos Velasco, Johannes Bühl, Ronny Engelmann, Martin Radenz, and Yin Zhenping

Leibniz Institute for Tropospheric Research (TROPOS), Leipzig, Germany

Correspondence: Hannes Jascha Griesche (griesche@tropos.de)

Abstract.

From 25 May to 21 July 2017, the research vessel Polarstern performed the cruise PS106 to the high Arctic in the region north and northeast of Svalbard. PS106 contributed observations for the initiative "Arctic Amplification: Climate Relevant Atmospheric and Surface Processes and Feedback Mechanisms (AC)[3]" which involves numerous projects aiming on under-

5 standing the role of atmospheric and surface processes in the ongoing rapid changes in the Arctic climate. As one of the central facilities of (AC)[3], the mobile remote sensing platform OCEANET was deployed aboard Polarstern. Within a single container, OCEANET houses state-of-the-art remote sensing equipment, including a multi-wavelength Raman polarization lidar Polly[XT] and a 14-channel microwave radiometer HATPRO. For the cruise PS106 the measurements were supplemented by a motion-stabilized 35-GHz cloud radar Mira-35.

10 This paper describes the treatment of technical challenges which were immanent during the deployment of OCEANET in the high Arctic. This includes the description of the motion stabilization of the cloud radar Mira-35 to ensure vertical-stare observations aboard the moving Polarstern. Also, low-level clouds and the presence of fog frequently prevented a continuous analysis of cloud conditions from synergies of lidar and radar within Cloudnet, because the technically determined lowest detection height of Mira-35 was 165 m above sea level. To overcome this obstacle, an approach for identification of the cloud

15 presence solely based on data from the near-field receiver of Polly[XT] at heights from 50 m and 165 m above sea level is presented.

In addition, we provide an overview of the data processing chain of the OCEANET observations and demonstrate case studies of aerosol and cloud studies to introduce the capabilities of the dataset. The retrieval of aerosol optical and microphysical properties from the observations of Polly[XT] is presented by means of observations performed during the ice floe camp. Syn-

20 ergies between the remote sensing instruments and auxiliary observations from aboard Polarstern were analyzed by means of Cloudnet which provides as primary output a target classification mask. This target classification is the basis for value-added products such as liquid- and ice-cloud microphysical properties, cloud dynamics which can in subsequent steps be used as input for the investigation of cloud microphysical processes, radiative transfer calculations, or model evaluation. To this end, new approaches for ice crystal effective radius and eddy dissipation rates have been implemented into Cloudnet.

1 Introduction

The Arctic is one of the hot spots of global climate change. This is observed as a change of several parameters such as the drastic decline of the Arctic sea ice (Meier et al., 2014). Also, in the past 30 years the mean Arctic near surface air-temperature anomaly increased at least by a factor of two faster compared to the global mean (Serreze and Barry, 2011). These phenomena, also summarized by the term Arctic Amplification, are assumed to be due to several feedback mechanisms, e.g., the surface

30 albedo feedback, lapse rate feedback, a change in the meridional atmospheric and oceanic mass and energy transport pattern, and an alteration in cloud cover, aerosol occurrence, and atmospheric moisture content (Wendisch et al., 2017). However, there is still a lack of understanding in the interplay of these feedback mechanisms as well as in quantifying their relative importance and magnitude (Serreze and Barry, 2011; Pithan and Mauritsen, 2014; Goosse et al., 2018).

The radiative effect of clouds is a major source of uncertainty in this matter. Arctic clouds have a high variability in their

35 radiative effects and in their impact on the surface energy balance (Yeo et al., 2018). The cloud-related radiative impacts have been found to be both positive (i.e., clouds have a warming effect) as well as negative (Goosse et al., 2018). A higher fraction of low clouds caused by a decreased sea ice extent increases the downwelling longwave radiation during polar night and thus induces a positive feedback. A higher fraction of liquid water in mixed-phase clouds due to a warmer climate, on the other hand was found to increase the cloud albedo. This in turn enhances the reflection of incoming shortwave radiation at the top

40 of the atmosphere during polar day (Goosse et al., 2018) and thus produces a negative feedback. Yet the underlying processes controlling Arctic cloud phase and occurrence, and hence the connected feedback mechanisms driving Arctic Amplification are not completely understood (e.g., Shupe et al., 2013; Kalesse et al., 2016a).

Though being a key requirement to study the Arctic energy budget, detailed observations of Arctic clouds still are rare. To study these clouds, different aircraft campaigns have been conducted in recent years in the Arctic (e.g., Curry et al., 2000;

45 Jacob et al., 2010; McFarquhar et al., 2011; Wendisch et al., 2019). While airborne measurements yield an unique, accurate description of the observed cloud, they lack the ability to measure the entire tropospheric column at once. This is a feature which active remote sensing observations can offer. Given this capability, ground-based remote sensing observations are suitable to investigate the spatio-temporal distribution of clouds (Bühl et al., 2013), their phase partitioning (de Boer et al., 2009; Zhang et al., 2014; Kalesse et al., 2016a), and their interaction with aerosols (Seifert et al., 2010). These data sets serve, e.g., as

50 basis for model evaluation (Illingworth et al., 2007; Neggers, 2019) and radiative transfer calculations (Barrientos Velasco et al., 2019; Ebell et al., 2019). Hence, additionally to the airborne campaigns, several shipborne campaigns equipped with remote sensing instrumentation have been conducted in the past years in the Arctic (e.g., Uttal et al., 2002; Tjernström et al., 2004; Tjernström et al., 2014; Granskog et al., 2018; Wendisch et al., 2019). Observations of space-borne cloud radar and lidar, as done aboard Cloudsat (Stephens et al., 2008) and CALIPSO (Winker et al., 2003) provide in addition a large-scale

55 overview of the Arctic cloud coverage (Liu et al., 2012). But the respective data sets lack information about the lowest cloud levels. Nevertheless, there are still only a few studies of sea-motion-stabilized cloud radars, whose availability is a necessary requirement to determine also cloud vertical dynamics accurately from a shipborne platform.

In order to study the feedback mechanisms causing Arctic Amplification, the initiative **ArctiC A**mplification: **C**limate Relevant Atmospheric and SurfaCe Processes and Feedback Mechanisms (AC)[3] conducted two complementary field campaigns in the Arctic summer of 2017: **A**rctic **CL**oud **O**bservations **U**sing airborne measurements during polar **D**ay (ACLOUD), an airborne campaign performed with the research aircraft Polar 5 and Polar 6, and the **P**hysical feedbacks of **A**rctic boundary layer, **S**ea ice, **C**loud and **A**eroso**L** (PASCAL) expedition deployed on and around the research ice breaker Polarstern (Macke and Flores, 2018; Wendisch et al., 2019). These campaigns took place in May and June 2017 in the regions north and northeast of Svalbard with the aim to combine remote sensing and in-situ observations. During PASCAL, a two-week ice floe camp was performed in the vicinity of Polarstern and a large number of auxiliary measurements were conducted on the ice. PASCAL was the first part of the split Polarstern cruise PS106 which lasted from 25 May until 21 July 2017. During the whole PS106 cruise, measurements with the multiwavelength polarization lidar Polly[XT]_OCEANET, a 35-GHz cloud radar Mira-35 and a microwave radiometer HATPRO (**H**umidity **A**nd **T**emperature **PRO**filer) of the OCEANET platform were conducted aboard Polarstern. Within (AC)[3] the OCEANET observations have the essential role to describe the temporal evolution of the vertical structure of aerosol and clouds in the Central Arctic. They constitute the prerequisite for further studies of aerosol-cloud interaction, model evaluation or radiative transfer modeling, which are partly covered by other subprojects of (AC)[3]. Scope of this study is thus to introduce the instrumentation and data analysis methods which are used to produce the OCEANET-based cloud and aerosol data sets for the cruise PS106.

In Section 2 of this paper, a detailed description of the OCEANET instruments and the auxiliary observations is given. The applied motion stabilization and heave rate correction of the cloud radar Doppler velocity, the data processing based on the synergistic Cloudnet algorithm (Illingworth et al., 2007) and the development of auxiliary retrievals for processing within Cloudnet are described in Sect. 3. In Section 4 the products derived from the OCEANET measurements using Cloudnet are illustrated by means of different case studies from the time period of the ice flow camp. The potential of Polly[XT]_OCEANET to characterize the free-tropospheric aerosol is also highlighted. In addition, a statistical overview about the observed cloud vertical structure with a special focus on low-level clouds during PS106 is presented. A final summary and conclusions are given in Sect. 5.

2 Instrumentation

During the complete PS106 campaign in the central Arctic in summer 2017 (see Fig. 1) a comprehensive number of remote sensing instruments was deployed aboard the research vessel (RV) Polarstern to conduct continuous observations of clouds and aerosol. To a large extent, these instruments were comprised in the OCEANET-Atmosphere observatory (Kanitz et al., 2013a). Additionally, auxiliary instruments for in-situ and remote sensing observations installed aboard Polarstern as well as during a two-week ice floe-camp, which was performed in the vicinity of the RV, were utilized for the studies presented in here. The first part of PS106 (PS106.1 / PASCAL) was accompanied by the ACLOUD aircraft campaign about both of which a brief overview is given by Wendisch et al. (2019).
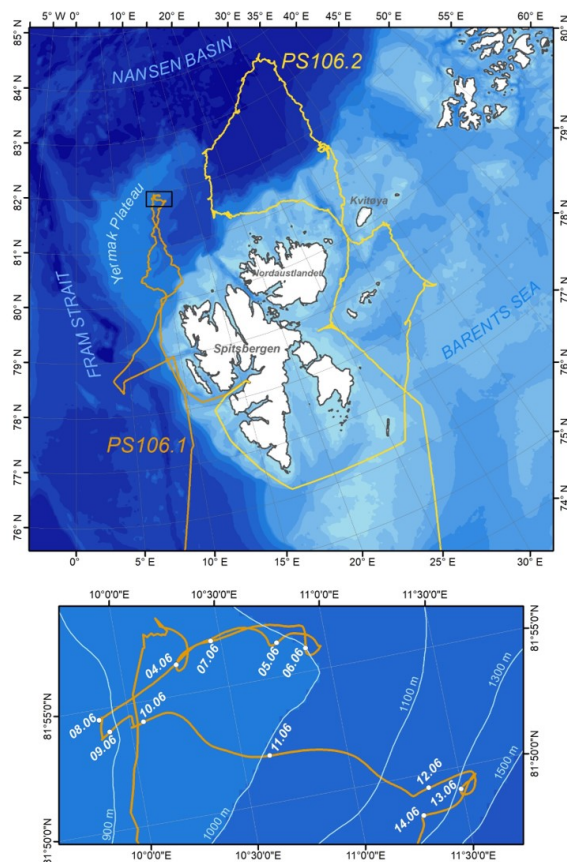
Figure 1. Track of RV Polarstern during PS106 (top). PASCAL (PS106.1) was the first part of PS106 and was accompanied by a two-week drift (zoom of inlet in the bottom subfigure) during which the ice floe camp was performed. Map by Anna Nikolopoulos.

90   The location of the OCEANET equipment and of the auxiliary Polarstern instruments deployed during PS106 that were used within this study are depicted in Fig. 2. Table 1 summarizes the technical details of the key equipment applied in the synergistic Cloudnet processing that is further described in Sect. 3.3. The different instruments will in the following be briefly introduced.

2.1   OCEANET

The OCEANET-Atmosphere observatory was already frequently operated aboard Polarstern (Kanitz et al., 2013b). Its con-
95 tainer is by default equipped with the multi-wavelength polarization Raman lidar Polly^{XT}_OCEANET (hereafter referred to as Polly^{XT}), to provide continuous profiles of cloud and aerosol properties (Engelmann et al., 2016). Additionally, a 14-channel microwave radiometer (MWR) HATPRO (Rose et al., 2005) for measurements of column-integrated liquid water and water vapor content and profiles of atmospheric temperature, a standard meteorological station, a pyranometer and a pyrgeometer for incoming short- and longwave radiation observations, as well as an all-sky camera for passive visible observations of the

Figure 2. Polarstern during the ice floe camp performed during the PASCAL campaign. Annotated are the locations of some selected instruments for atmospheric measurements. (1–5) indicate the positions of the key instruments used for Cloudnet processing: Polly^{XT}, HATPRO, Mira-35, disdrometer and radiosondes. (6) denotes one of the 15 pyranometers comprising pyranometer network, at (7) was the tethered balloon launching site and at (8) aerosol in-situ measurements had been conducted. (1–3) are permanent part of OCEANET.

100 full sky were installed. During PS106, OCEANET was complemented for the first time with a vertically-pointing motion-stabilized 35-GHz polarimetric Doppler cloud radar of type Mira-35 (Görsdorf et al., 2015) for continuous vertically resolved measurements of Doppler spectra produced by cloud vertical motions.

The Polly^{XT} system measures profiles of particle backscatter coefficient at three wavelengths (355, 512 and 1064 nm), and of extinction coefficient as well as of the linear depolarization ratio at two wavelengths (355 and 512 nm), respectively.

105 Four near-field channels for detection of elastically and Raman-scattered light from nitrogen molecules are implemented at 355, 387, 532 and 607 nm to enable observations already at low heights starting at about 50 m above the instrument. An additional channel for detection of Raman-scattered light from water vapor at 407 nm allows the retrieval of the water vapor mixing ratio (Dai et al., 2018) during low sunlight conditions. From the Polly^{XT} backscatter and extinction measurements, aerosol classification by their optical properties (Müller et al., 2007; Baars et al., 2017) up to the retrieval of particle size

110 distribution and number concentration (Müller et al., 1999; Baars et al., 2012) can potentially be derived. The polarization-sensitive detection channels allow to determine the shape of the observed aerosol and cloud particles (Kanitz et al., 2013a) and, for instance, to separate dust and non-dust particles in mixed aerosol layers (Baars et al., 2011). By applying the shape-detection capabilities of the polarization channels for the discrimination of spherical liquid droplets from non-spherical ice particles, heterogeneous ice formation in mixed-phase clouds can be studied (Seifert et al., 2015). Another application of depolarization

115 observations in mixed-phase cloud studies is the estimation of cloud condensation nuclei (CCN) and ice nucleating particle (INP) concentrations (Mamouri and Ansmann, 2016). Due to the relatively short wavelengths of the lidar compared to the cloud radar, it follows that the lidar is sensitive to rather small particles such as aerosol or small cloud droplets. Also attenuation, especially due to liquid clouds, has to be considered.

The MWR HATPRO provides estimates of the liquid water path (LWP), integrated water vapor (IWV), as well as humidity and temperature profiles with a temporal resolution of 1 Hz. The MWR measures the emission of radiation from the atmosphere in two frequency bands ranging from 22.24 – 31.4 GHz and from 51.0 – 58.0 GHz at 14 different channels. The MWR datasets shown in this study are based on a retrieval that was created based on a long-term radiosonde dataset from De Bilt, NL (52°06' N, 5°11' E, 4 m hasl, WMOCode 6260) according to Löhnert and Crewell (2003). We are aware of possible differences that may arise by applying a mid-latitude retrieval to Arctic measurements but do think that the atmospheric conditions in summer in the Arctic are comparable to those in winter in the Netherlands. Nevertheless the preparation of an Arctic retrieval based on ERA-Interim data is in progress.

During PS106, the Ka-band Doppler radar Mira-35 was set-up to emit pulses with a width of 208 ns at a pulse repetition frequency of 5000 Hz. This corresponds to a vertical resolution of 31.18 m. The upper limit of the measurement range was set to 15 km. The Doppler spectrum was derived from the backscattered signals of 256 consecutive pulses. To allow the correction of the cloud radar data for the vessel movement, the whole spectrum (including noise) has been stored with a temporal resolution of 4 Hz and a Doppler resolution of 0.08 m s^{-1}. This correction has been done in a post processing procedure which is explained in Sect. 3.1. From the profiles of the Doppler spectra, the different Doppler moments such as radar reflectivity, Doppler velocity, and Doppler spectral width were determined as described in Görsdorf et al. (2015). The linear depolarization ratio (LDR) was obtained from the ratio of the radar reflectivity factor observed in the co- and cross-channels of Mira-35 and provides information about the hydrometeor shape (Bühl et al., 2016). In contrast to the lidar, the longer wavelength of operation of the cloud radar defines its sensitivity to range from cloud hydrometeors to slight precipitation. Especially in the case of shallow stratiform clouds, as they dominated the measurements during PS106, attenuation effects can be neglected. The OCEANET datasets of HATPRO, Polly^{XT} and Mira-35 are publicly available through the Open Access library PANGAEA (Griesche et al., 2019b, c, d).

2.2 Auxiliary instrumentation

Added value of the OCEANET measurements can be obtained when they are accompanied by additional observations. During the two-week ice floe camp performed in the frame of PASCAL, a tethered balloon site was set up for turbulence and radiation observations (Egerer et al., 2019) and a network covering 15 pyranometers to determine the spatial variability of the solar radiation was installed (Barrientos Velasco et al., 2019). In the context of this study, the turbulence as determined from the three-dimensional wind vector measured with high temporal resolution of several tens of Hertz by an ultrasonic anemometer attached to the tether of the balloon was used. To obtain mass and number concentration as well as optical properties and filter samples of the aerosol at the surface, a container equipped with instrumentation for aerosol in-situ measurements was installed on the deck of Polarstern and was measuring continuously during the whole two-month cruise (Kecorius et al., 2019). Also aboard Polarstern, measurements of the optical thickness of the cloud-free atmosphere were performed using a hand-held Solar Light Microtops Sun photometer. The Sun photometer measurements are already available through the AErosol RObotic NETwork (AERONET) project. An optical disdrometer, which is part of the OceanRAIN network (Klepp et al., 2018), mounted on the crows nest of the RV was continuously measuring the precipitation rate for different hydrometeor types and size bins.

Table 1. Overview of the ship-borne remote sensing instrumentation deployed during PS106 that had been used for processing of the Oceanet observations.

Instrument Type	Reference	Measured Quantities	ν: Frequency λ: Wavelength R: Range of Measurement P: Precision	Time Resolution
Raman Lidar PollyXT	Engelmann et al. (2016)	Particle backscatter coefficient	$\lambda = 355, 532, 1064\,\mathrm{nm}$; R: 0.1–15 km, 0–1 km^{-1} sr^{-1} P: 7.5 m; 1e-5 km^{-1} sr^{-1}	10 min - 1 hour
		Particle extinction coefficient	$\lambda = 355, 532\,\mathrm{nm}$ R: 0.3–5 km, 0–10 km^{-1} P: 300 m; 1e-2 km^{-1}	
		Particle linear depolarization ratio	$\lambda = 355, 532\,\mathrm{nm}$ R: 0.1–15 km, 0–0.5; P: 7.5 m; 0.02	
Microwave Radiometer RPG HATPRO-G2 first generation dual profiler	Rose et al. (2005)	Integrated water vapor (IWV)	$\nu = 22.24$–31.4 GHz R: 0–35 kg m^{-2} P: 0.2 kg m^{-2}	1 Hz
		Liquid water path (LWP)	$\nu = 22.24$–31.4 GHz R: 0–1 kg m^{-2} P: 0.02 kg m^{-2}	
		Brightness temperature (TB)	$\nu = 51.0$–58.0 GHz R: 0–330 K P: 0.2–1 K	
Doppler Cloud Radar Metek Mira-35	Görsdorf et al. (2015)		$\nu = 35.5$ GHz	3.5 sec
		Radar reflectivity factor	R: 150–13000 m; -55–20 dBZ P: 3 m; 2 dBZ	
		Linear depolarization ratio	R: 150–13000 m; -26-0 dB P: 30 m; 1 dB	
		Hydrometeor vertical velocity	R: 150–13000 m; -11–11 m s^{-1} P: 30 m; 0.08 m s^{-1}	
Optical Disdrometer Eigenbrot ODM470	Klepp et al. (2018)	Particle size distribution	$\lambda = 880\,\mathrm{nm}$; R: 0.04–22 mm; P: 0.03–0.5 mm	1 min

Additionally, launches of Vaisala RS92-SGP radiosondes were conducted every 6 hours (shortly before 5, 11, 17 and 23 UTC to reach 100 hPa approximately at 6, 12, 18 and 24 UTC) to obtain in-situ profiles of temperature, relative humidity, pressure, and horizontal wind speed and direction.

3 Data processing and synergistic retrievals

Aim of the OCEANET observations from PS106 was to provide a continuous vertically-resolved view on cloud and aerosol macro- and microphysical properties in order to enhance the understanding of the Arctic atmosphere system and to support partner projects with datasets for radiative transfer calculations and turbulence studies. To derive continuous products of cloud
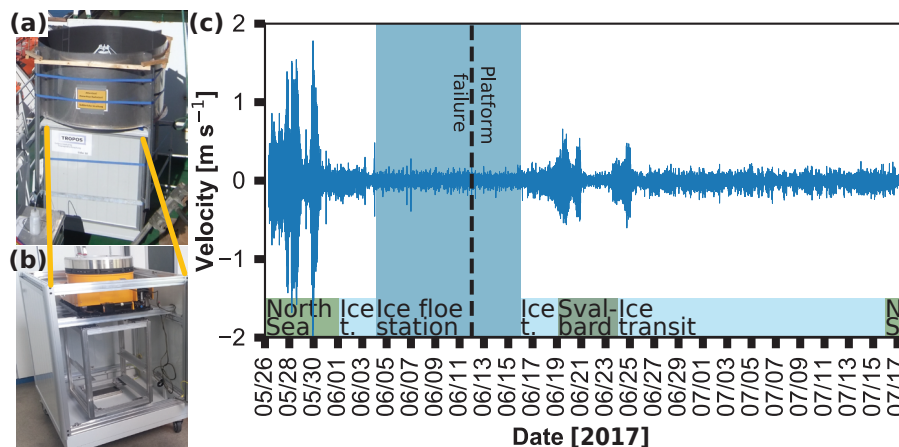
Figure 3. (a) The cloud radar aboard Polarstern (a) and the stabilization platform (b). (c) shows the time series of the cloud radar heave rate during PS106, an overview of the respective area where Polarstern was located. The dashed vertical line indicates the moment when the stabilization platform got a malfunction. At the bottom a rough localization of Polarstern is annotated (green: North Sea (N.S.), light blue: Ice transit (Ice t.), dark blue: Ice floe camp, dark green: Svalbard region (Svalbard)).

and aerosol properties, the shipborne OCEANET remote sensing observations were processed using the synergistic retrieval algorithm Cloudnet (Illingworth et al., 2007). In this section, we describe the extension of the standard Cloudnet algorithms by additional simple but operationally applicable products providing estimates of cloud droplet and ice crystal effective radius and the cloud-turbulence parameter eddy dissipation rate (EDR). The procedure for minimizing the influence of the RV motion
165 on the measurement of vertical velocities with Mira-35, which are required for the EDR retrieval, is also explained below.

3.1   Correction of vertical-stare cloud radar observations for ship motion

A structural requirement to derive valid vertical velocity from a Doppler cloud radar is a vertical pointing radar without an own vertical-velocity component. When the cloud radar is pointing off-zenith, the measured vertical-stare Doppler velocity will be biased by an additional component introduced by the horizontal wind. Based on high resolved horizontal wind data
170 and the radar beam incident angle, a correction is possible for this bias (Wulfmeyer and Janjić, 2005). For PS106, a different approach was chosen. Similar to the approach described by Achtert et al. (2015), the cloud radar was mounted on an active stabilization platform (Fig. 3 (b)), which was in our case a predecessor of the SOMAG AG Jena – GSM 4000 (SOMAG, 2017). This platform actively leveled out the roll and pitch movement of the RV in a way that no correction of horizontal-wind effects was necessary. On the other hand, if the cloud radar itself moves in a vertical direction, the resulting velocity superimposes the
175 measured Doppler velocity. In the case of a moving RV, the vertical movement is induced by the RVs heave rate and rotation. The necessary heave correction was done in a post-processing procedure which will now be introduced.

To enable the correction, the complete radar Doppler spectra as well as the motion data (rotation and translation) of Polarstern were stored with a resolution of 4 Hz and 20 Hz, respectively, throughout the entire cruise. The heave rate of the cloud radar
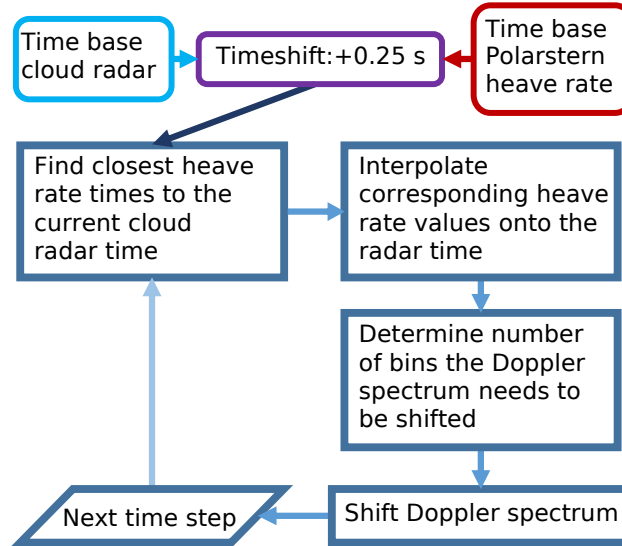
Figure 4. Flowchart of the heave rate correction.

v_{C_z} was determined by summing up the z-component of the cross product between the rotation vector of Polarstern $\boldsymbol{v_{P_R}}$ and

180 the position of the radar $\boldsymbol{X_R}$ relative to the mass centre of the RV

$$
\boldsymbol{v_R} = \boldsymbol{v_{P_R}} \times \boldsymbol{X_R} = \begin{pmatrix} P_{pitch} \\ P_{roll} \\ P_{yaw} \end{pmatrix} \times \begin{pmatrix} x_R \\ y_R \\ z_R \end{pmatrix} = \begin{pmatrix} v_{R_x} \\ v_{R_y} \\ v_{R_z} \end{pmatrix} \tag{1}
$$

with the z-component of the translation vector of Polarstern $v_{P_{T,z}}$

$$
v_{C_z} = v_{R_z} + v_{P_{T,z}}. \tag{2}
$$

In Figure 3 (b) the time series of v_{C_z} for PS106 is shown. The heave rate correction was done by shifting each individual

185 Doppler spectrum opposite to the cloud radar heave rate. An illustration of this procedure is shown in Fig 4. In an initial

step, the cross correlation between the timestamps of the two data sets, the cloud radar Doppler spectrum and the cloud radar

heave rate, was calculated to check for a possible time shift between both datasets. This was found to be 0.25 s. Subsequently,

the two values of v_{C_z} from before and after the current Doppler spectrum have been linearly interpolated onto its respec-

tive time. Finally, the spectrum was shifted according to the number of spectral bins determined by the Doppler resolution (

190 $\Delta v_{DopplerSpectrum} = 0.08\,\mathrm{m\,s^{-1}}$) and the interpolated heave rate.

The effect of the heave correction is illustrated in Figure 5. In Figure 5 (a) the uncorrected Doppler velocity measured on

30 May 2017 between $00{:}00 - 01{:}00$ UTC, together with the respective histogram of the velocities is shown. The RVs movement
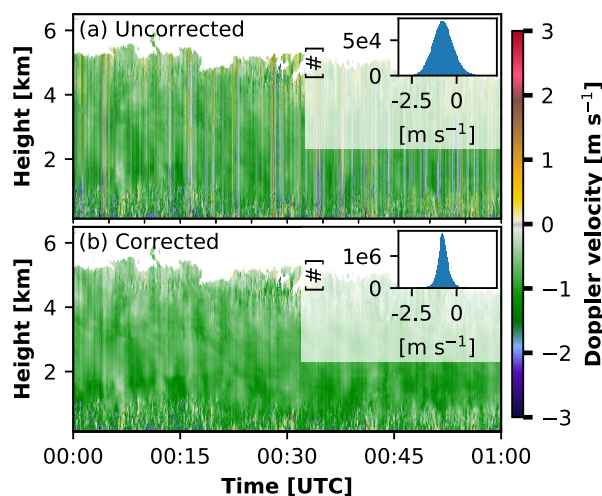
Figure 5. Uncorrected (a) and corrected (b) Doppler velocity during PASCAL on 30 May 2017 between 00:00 – 01:00 UTC. In the small box in the upper right corner the respective histogram of the presented Doppler velocity is shown. Negative values denote downward motion.

is visible in both, in the time-height cross-section of the Doppler velocity as stripes of enhanced or reduced velocity throughout the whole column as well as in the broadening of the histogram. The same is presented in Fig. 5 (b) but for the corrected Doppler velocity.

3.2 Retrieval of eddy dissipation rate

The rate at which turbulence kinetic energy is transferred from larger eddies into smaller ones and eventually dissolve into thermal energy is the EDR. This is used as a quantitative proxy of atmospheric turbulence. Several approaches to retrieve the EDR are common. Methods exist for in-situ measurements from aircraft- (Nicholls, 1978; Nucciarone and Young, 1991; Meischner et al., 2001), helicopter- (Siebert et al., 2006a), and balloon-borne (Caughey et al., 1979; Siebert et al., 2006b), as well as for meteorological tower instruments (Caughey et al., 1979; Kaimal et al., 1976; Zhou et al., 1985). Additional retrievals for remote sensing observation have been developed (Borque et al., 2016; Sathe and Mann, 2013). These methods are based on the Doppler velocity structure function derived from vertically-pointed Doppler lidar (Frehlich and Cornman, 2002) or Doppler radar (Lothon et al., 2005) or a combination of the width of the Doppler spectrum and the Doppler velocity measurements (Meischner et al., 2001). Other retrievals use time series analyses of vertical velocities from vertical-stare Doppler radar (Shupe et al., 2012; Kalesse and Kollias, 2013) or Doppler lidar observations (O'Connor et al., 2010).

Typical values for EDR in clouds spread between $10^{-1} - 10^{-8}$ m^2 s^{-3}. Borque et al. (2016) report EDR of maritime and continental stratiform clouds in the order of $10^{-4} - 10^{-2}$ m^2 s^{-3} and $10^{-7} - 10^{-2}$ m^2 s^{-3}, respectively. In cumulus clouds with weak updrafts, EDR had been found in a range between $5 \cdot 10^{-5} - 10^{-2}$ m^2 s^{-3}, whereas values up to 10^{-1} m^2 s^{-3} were found for cumulus clouds with strong updrafts (Siebert et al., 2006a). In cumulonimbus clouds, Meischner et al. (2001) found values

for EDR between $10^{-6} - 5 \cdot 10^{-2}\,\mathrm{m^2\,s^{-3}}$. For low clouds or fog at Chilbolton, UK, O'Connor et al. (2010) estimated the EDR to be in the order of $10^{-4} - 5 \cdot 10^{-2}\,\mathrm{m^2\,s^{-3}}$.

The presented range of EDR for different cloud conditions suggests that also Arctic clouds might show characteristic differences for varying atmospheric conditions. The vertical alignment of the cloud radar during PS106 enables the determination of EDR from the vertical air motions observed in cloud layers. Below, we thus present a retrieval technique for EDR that can be applied to the OCEANET data set.

3.2.1 EDR from vertical-stare Doppler velocity power spectra

Assuming the turbulent energy dissipation is a homogeneous and isotropic process, the turbulent energy spectrum $S(k)$ within its inertial subrange is represented according to Borque et al. (2016) by

$$S(k) = A\varepsilon^{2/3} k^{-5/3}, \tag{3}$$

with $A = 0.5$ the Kolmogorov constant for a 1-D wind spectra (Sreenivasan, 1995). k represents the wavenumber, which is related to a length scale L ($k = 2\pi/L$) as well as to frequency f with $k = f/V_h$ and V_h as the horizontal wind speed and assuming a linear wind field. If in a log-log plot the observed spectra within the inertial subrange follows a $-5/3$ slope, ε can be estimated by

$$\varepsilon = \left(\frac{10^{k_0}}{A}\right)^{3/2} \tag{4}$$

where k_0 is the corresponding intercept of the linearized fit.

For this study, power spectra of the Doppler velocity with 4 Hz of continuous time series covering 5 minutes were calculated. To get the best estimate of the respective inertial subrange, the fit was determined by calculating a linear least-squares regression of the spectrum in 34 different wavenumber intervals. The corresponding wavenumber intervals Δk_i are depicted in Fig. 6 (a) together with the spectrum of the verrtical velocity observed on 7 June 2017, from 10:28 - 10:43 UTC. Following Borque et al. (2016), a good fit was defined with a slope from the linear regression of -5/3 ± 20% (-5/3 ± 1/3). If this criteria was matched within more than one wavenumber interval the mean of all ε_i for one spectrum was calculated. In order to evaluate the EDR estimated by cloud radar measurements, it was compared to EDR derived from the tethered balloon (Egerer et al., 2019). The time periods used for deriving EDR from the tethered balloon was 15 minutes, during which it was located at a constant height above ground. Two comparisons had been done, one on 7 June 2017, between 10:28 and 10:43 UTC and one on 9 June 2017, between 09:00 and 09:15 UTC.

In Figure 6 (a) an intercomparison of the power spectrum derived by the tethered balloon measurements (red) with the spectrum as it was derived from the cloud radar (blue) according to the techniques described above is shown for the period on 7 June 2017. The comparisons of the two retrievals showed that the values differ by a factor of 2–3. For 7 June, the cloud radar retrieval underestimated the balloon value (Fig. 6 (a)) and vice versa for 9 June (not shown here). This discrepancy is in the order of magnitude as one could expect due to the spatial distance between the two measurements alone (about 200 m). The
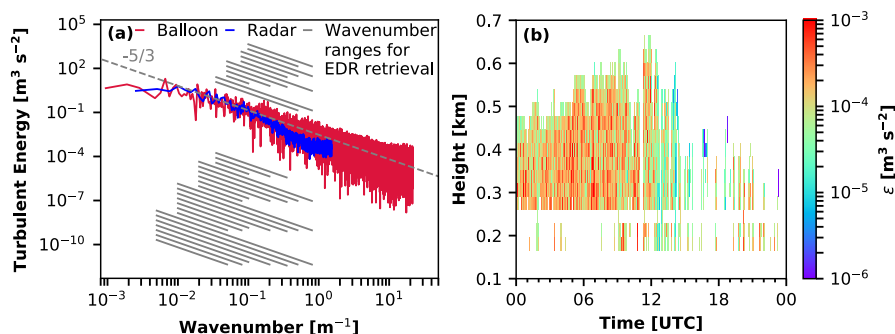
Figure 6. (a) Fourier spectrum derived from cloud radar Doppler velocities (blue) and from tethered balloon (red) turbulence measurements on 7 June 2017 between 1027–1043 UTC at 380 m height. The EDR values of the two methods were: $\varepsilon_{TetheredBalloon} = 2.65 \cdot 10^{-4} \, \mathrm{m^2 s^{-3}}$ and $\varepsilon_{CloudRadar} = 6.84 \cdot 10^{-4} \, \mathrm{m^2 s^{-3}}$. Grey lines: Illustration of the wavenumber intervals that had been used to check for a -5/3 slope of the Fourier spectrum. Dashed line: example for -5/3 slope. (b) shows the time-height cross-section of EDR on 7 June 2017, as derived from the cloud radar observations.

dashed line in Fig. 6 (a) is an example for the -5/3 slope and the black lines indicate the wavenumber intervals that had been used to check for a -5/3 slope of the Fourier spectrum.

Figure 6 (b) displays the time-height cross sections of EDR on 7 June 2017 between $100 - 800 \, \mathrm{m}$ height. Until 12:00 the
245 EDR was rather high with values up to $10^{-3} \, \mathrm{m^2 s^{-3}}$. After that, the EDR decreased rapidly down to values below $10^{-4} \, \mathrm{m^2 s^{-3}}$ and eventually the cloud dissolved.

3.3 Cloud macro- and microphysical properties from instrument Synergies

To acquire a data set suitable for the statistical evaluation of the macro- and microphysical properties of clouds observed during PS106, the instrument synergistic approach Cloudnet (Illingworth et al., 2007) was applied. This data set in addition
250 serves to realize model evaluations (Illingworth et al., 2007) and radiative transfer calculations, e.g, with the Rapid Radiative Transfer Model for climate and weather models (RRTMG; Iacono et al. (2008)). RRTMG is currently utilized for single column radiative transfer calculations. The model considers vertical profiles of relative humidity and temperature, standard atmospheric constituent profiles based on Anderson et al. (1986) and cloud macro and microphysical properties of clouds. These assignments include sets of effective radius and mass concentration of liquid and ice hydrometeors. In the following, the
255 approaches for achieving these dataset requirements based on the PS106 remote-sensing observations are described.

3.3.1 Cloudnet

The instrument synergy approach Cloudnet (Illingworth et al., 2007), which combines the observations from lidar, cloud radar, microwave radiometer, disdrometer and radiosondes was used to determine cloud physical properties during PS106. To illustrate this procedure, the Cloudnet approach will now be briefly introduced. The measurements are first averaged on a common

260 grid with a vertical and temporal resolution of 31.18 m (resulting from the cloud radar resolution) and 30 s, respectively. Based on the observations scaled on the Cloudnet grid, a classification mask is derived, which assigns a series of 7 distinct features to the observed targets: clear yes/no; liquid yes/no; falling yes/no; wet bulb temperature below 0 °C yes/no; melting layer yes/no; aerosol yes/no; insects yes/no. The bitwise classification ensures that each data point is characterized by a defined combination of these features. Based on the individual combination of the classification bits, a set of typical atmospheric targets is derived,

265 as described by Hogan and O'Connor (2004).

Cloud droplets are assumed to be spherical and to have a large effective surface compared to ice crystals as they are in fact rather small but appear in high number. Their presence is determined by lidar measurements due to its sensitivity to small-sized but numerous particles. Hence a Cloudnet pixel with high backscatter and a distinct decrease after the signal is defined as liquid. The presence of ice is determined by a radar pixel indicating a falling particle at a dew point temperature $T < 0$ °C. If both

270 criteria for liquid and ice, high lidar backscatter, and downward-pointing cloud radar vertical velocity are fulfilled at $T < 0$ °C the pixel is identified as mixed-phase. Besides using the air temperature, the melting layer is also identified by a cloud radar linear depolarization ratio LDR > -15 dB or a strong increase of the vertical velocity observed by the cloud radar. To estimate the temperature at the respective time-height pixel, radiosonde-based profiles of thermodynamic variables are interpolated on the Cloudnet grid. If no radiosonde was launched from the RV but Polarstern was in the vicinity of Svalbard, soundings from

275 Ny Ålesund (Maturilli, 2017) were substitutionally utilised. As a last fall-back option, data from the Global Data Assimilation System model (GDAS) with a horizontal and vertical resolution of 1° and 3 h (GDAS1) was used as meteorological input into Cloudnet. Due to their rather small size but heterogeneous shape, aerosols are characterized by absence of a radar signal and low lidar backscatter signals which can show both strong or weak depolarization, depending on the aerosol type (Baars et al., 2017).

280 Besides the phase of the cloud, the respective mass concentrations of ice and liquid water are determined were applicable. The liquid water content (LWC) is derived by scaling the MWR liquid water path adiabatically onto the cloud pixels defined as liquid or mixed-phase (Frisch et al., 1998; Merk et al., 2016). For pure-liquid data points, the approach of Frisch et al. (2002) is used to derive the cloud droplet effective radius from the observed radar reflectivity factor and liquid water path and an assumed width of the log-normal cloud droplet size distribution (which was, according to Miles et al. (2000), set to 0.35 in our

285 study). The ice water content (IWC) is calculated using an empirical formula from Hogan et al. (2006) relating cloud radar reflectivity Z and temperature T. This approach for IWC is only applied for those clouds Cloudnet classified as ice clouds. In this step also a correction for potential attenuation of the cloud radar signal due to the presence of liquid water is made. Dealing with thin Arctic clouds, this was no big issue for this study.

3.3.2 Ice crystal effective radius

290 As discussed above, Cloudnet offers a variety of retrievals for ice microphysical parameters. Nevertheless, the continuous application of radiative transfer calculations requires a consistent availability of ice and liquid hydrometeor effective radius and mass concentration. While Cloudnet already contains retrievals for effective radius and mass concentration of liquid droplets, as well for ice water content, so far no operational retrieval for ice effective radius is available. We therefore decided for the

implementation of a new approach which is based on the combination of a definition of the effective radius as the ratio of the
295 third to the second moment of the particle size distribution (PSD) and an empirical relationship between the visible extinction
coefficient α, cloud radar reflectivity, and model temperature. Similar as for IWC (and α), $r_{e_{ice}}$ is only calculated for datapoints
where Cloudnet classified ice clouds.

Using the ratio of the second to the third moment of the PSD, the effective radius $r_{e_{ice}}$ can be related to IWC and α (Delanoë
et al., 2007). This yields for $r_{e_{ice}}$:

$$300 \quad r_{e_{ice}} = \frac{3}{2} \frac{IWC}{\rho_i \alpha} \cdot 10^6 \ (\mu m), \tag{5}$$

with ρ_i as density of the solid ice ($\rho_i = 917\,\mathrm{kg\,m^{-3}}$). Both, IWC and α have been calculated using empirical relationships
between IWC or α, and the cloud radar reflectivity Z of a 35-GHz cloud radar and temperature T (Hogan et al., 2006).

Finally, we found for the ice crystal effective radius a Z-T relationship:

$$r_{e_{ice}} = \frac{3}{2\rho_i} 10^{C_{ZT} \cdot ZT + C_Z \cdot Z + C_T \cdot T + C} \cdot 10^6 \ (\mu m), \tag{6}$$

305 with $C_{ZT} = -2.05 \cdot 10^{-4}$, $C_Z = 1.6 \cdot 10^{-3}$, $C_T = -1.71 \cdot 10^{-2}$ and $C = -1.52$.

To estimate the error of the identified effective radii of the ice crystals, an error propagation of Eq. (6) had be done using the
respective error for IWC and α from Hogan et al. (2006).

3.3.3 Fog detection

During PS106, frequently low-level clouds (cloud base < 165 m) or fog have been observed. These situations were often as-
310 sociated with an attenuation of the lidar beam within the lowest few hundred meters above Polarstern due to the high optical
thickness of these clouds. The cloud radar, in turn, has its technical limitation in detecting the lowest part of the boundary
layer. The measurements of Mira-35 start in a height of 155 m above the instrument. Due to the instrument synergy approach
of Cloudnet this is also the height of the lowest Cloudnet data pixel. Thus, the low-level clouds which occurred during PS106
introduced on the one hand issues to the Cloudnet retrieval due to misinterpretation of attenuated lidar signal as missing signal.
315 On the other hand, since most current statistics of Arctic clouds do not consider clouds in such a low altitude, these clouds
tend to be underrepresented in Arctic cloud statistics. To address these issues, we introduce a new Cloudnet classification
category called fog. Fog was identified by the Polly$^{\mathrm{XT}}$ signal-to-noise ratio (SNR, (Heese et al., 2010)) in the lowest 165 m
above sea level. If the SNR exceeded a value of 40 this was assumed to be due to the presence of fog. Since the SNR is not
yet range-corrected, this threshold-crossing at these low altitudes is very likely only due to the occurrence of fog or low-level
320 clouds.

3.4 Retrieval of CCN- and INP number concentrations

Arctic clouds and their susceptibility to the presence of aerosol are still in focus of research (Morrison et al., 2012). Based on the measurements of Polly[XT], an estimation of cloud condensation nuclei (CCN) and ice nucleating particle (INP) properties is possible (Mamouri and Ansmann, 2016). To do so, profiles of the aerosol backscatter coefficient and depolarization ratio

325   need to be determined. In a second step, these profiles are converted into profiles of the particle extinction coefficient using an appropriate lidar ratio (extinction-to-backscatter ratio).

The CCN number concentration (CCNC) and INP number concentration (INPC) profiles were estimated from profiles of the lidar-derived particle extinction coefficient at 532 nm by means of conversion parameters and published INP parameterization schemes (DeMott et al., 2010) as described by Mamouri and Ansmann (2016). The required conversion parameters for Arctic

330   AERONET stations were determined in the same way as outlined by Mamouri and Ansmann (2016). We used multi-year (2004-2017) Sun-photometer observations of the AERONET stations Thule, PEARL, Kangerlussuaq, Ittoqqortoormiit, and Hornsund to obtain the set of Arctic conversion parameters. These AERONET observations were made during the summer half years.

The direct retrieval of the CCN conversion parameters from the AERONET data (level 2, version 3, inversion products)

335   revealed $C_1 = 18.6\,\mathrm{cm}^{-3}$ and exponent $d_1 = 0.83$ for the range of extinction coefficients from $15 - 300\,\mathrm{Mm}^{-1}$ (500 nm AOD from $0.015 - 0.3$ were measured). During the PS106 observations, the aerosol extinction coefficient was mostly around 1–$10\,\mathrm{Mm}^{-1}$ in the lower part of the troposphere. The AERONET data for this low range of extinction coefficients indicates that conversion parameters of $C_2 = 10\,\mathrm{cm}^{-3}$, $d_2 = 0.9$, $C_3 = 3.0\,\mathrm{cm}^{-3}$, $d_3 = 1$ would be appropriate. The aerosol in the Arctic is fine-mode dominated and shows Ångstrom exponents (440–870 nm) typically between 0.9 and 1.8 (with an average of 1.5–1.6).

340   ### 3.5 Back trajectory analysis: Trace

To analyse the origin of an observed air mass and to classify the most likely continental source region, the trajectory analysis tool Trace based on HYSPLIT (Stein et al., 2015) and GDAS1 data as dynamic driver were used. This trajectory analysis tool calculates 10-day backward trajectories of an 27-member trajectory ensemble. To estimate the most likely source region of the trajectory, the residence time below the mixing depth provided by the GDAS1 data set was used and categorized in different

345   land cover categories (Foth et al., 2019; Radenz and Seifert, 2019).

4 Results

4.1 Case studies

Three case studies will be presented in the following. They were, on the one hand, chosen to demonstrate the potential OCEANET offers, by presenting the capabilities of the standard Cloudnet products and of Polly[XT]. On the other hand, these

350   cases are selected to illustrate the new products introduced in this study.
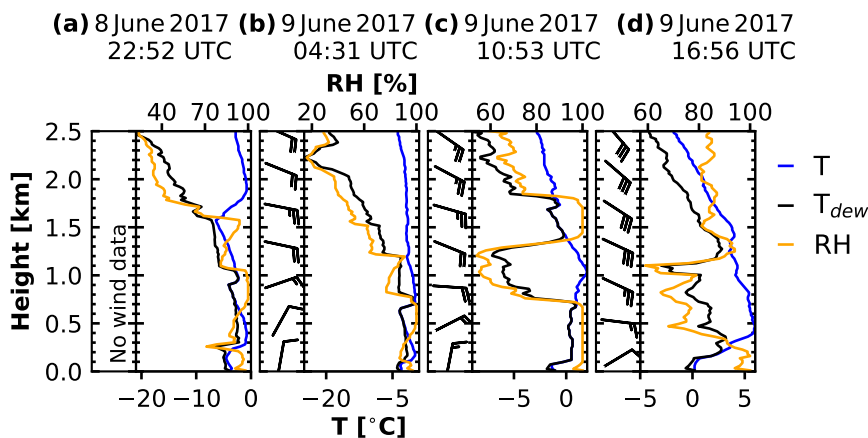
Figure 7. Thermodynamic profiles from radiosondes launched aboard Polarstern on (a) 8 June 2017 at 22:52 UTC, (b) 9 June 2017, 04:31 UTC, (c) 9 June 2017, 10:53 UTC, and (d) 9 June 2017,16:56 UTC. Each sounding is divided into two parts: left side the wind barbs, right side the temperature (blue), dew point temperature (black), and relative humidity (orange) profiles.

4.1.1 Precipitating layered cloud: 9 June 2017, 00:00 – 18:00 UTC, ice floe camp

An overview of the capability of the OCEANET measurements and its application to analyze cloud and aerosol structures and their interactions will be presented for a complex case that occurred over Polarstern on 9 June 2017 between 00:00 – 18:00 UTC. The radiosonde profiles for this period are shown in Fig. 4.1.1 up to a height of 2000 m. The observations of the cloud radar, the lidar and the MWR are depicted in Fig. 8.

The presented day reveals a rather complex situation. Starting at 00:00 UTC, Cloudnet classified a liquid stratocumulus layer between 600 – 900 m height with a cloud top temperature of -1.5 °C. This layer slowly descended, reaching a cloud base of about 400 m and cloud top of about 800 m at 05:00 UTC. The LWP during this period was rather constant with a mean value of $50 \, \mathrm{g \, m^{-2}}$ with two distinct peaks: one at around 01:50 UTC and the other one around 04:45 UTC with a LWP of up to $70 \, \mathrm{g \, m^{-2}}$, both associated with a slight increase in cloud depth. The constantly high values of EDR until roughly 05:00 UTC ($10^{-4} - -10^{-3} \, \mathrm{m^2 s^{-3}}$, Fig. 9 (d)) indicate strong turbulent mixing of the cloud layer.

At around 05:30 UTC, a transformation of the cloud occurred, the LWP increased up to $160 \, \mathrm{g \, m^{-2}}$ and precipitation started, almost reaching the ground (the disdrometer aboard Polarstern showed no precipitation signal, not shown here). Though the LDR showed no increased values, the presence of ice was identified due to detection of enhanced radar reflectivity and vertical velocity and thus a mixed-phase cloud was classified between 05:30 – 06:30 UTC. During this period, the retrievals of the ice and liquid hydrometeor size as proposed in this paper may be influenced by each other. Both retrievals are based on the same quantity, the radar reflectivity, which is characterized by the largest peak in the Doppler spectrum. To tackle this issue, a peak separation of the Doppler spectrum as it is proposed e.g., by Shupe et al. (2004), Kalesse et al. (2016b) or Radenz et al. (2019) would be necessary. This would offer the opportunity to calculate the effective radius of the different hydrometeors species
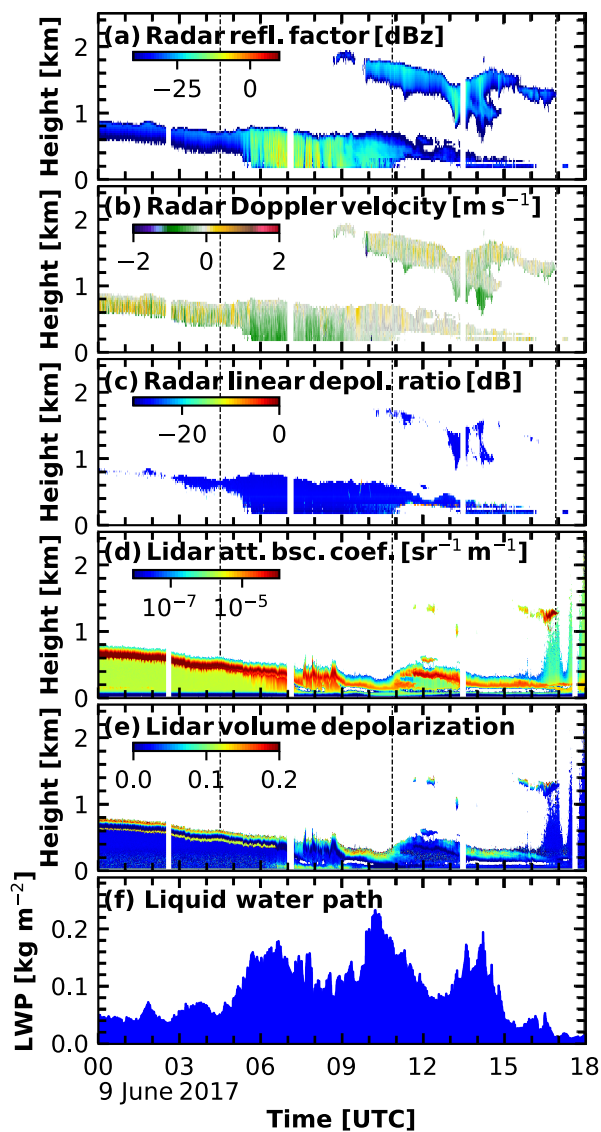
Figure 8. OCEANET observations on 9 June 2017 between 00:00 – 18:00 UTC. (a), (b) and (c) show the radar reflectivity factor, Doppler velocity, and linear depolarization ratio, respectively. (d) and (e) depict the lidar attenuated backscatter coefficient at 1064 nm and volume depolarization ratio at 532 nm, respectively. In (f) the liquid water path derived by the microwave radiometer is shown. The dashed vertical lines mark the time of the radiosonde launches on 9 June 2017 (note: the time of the first launch shown in Fig. 4.1.1 was before the plotted profiles of the measurements start).

370   based on their particular reflectivity but is beyond the scope of this paper. At around 06:30 UTC the interpolated temperature
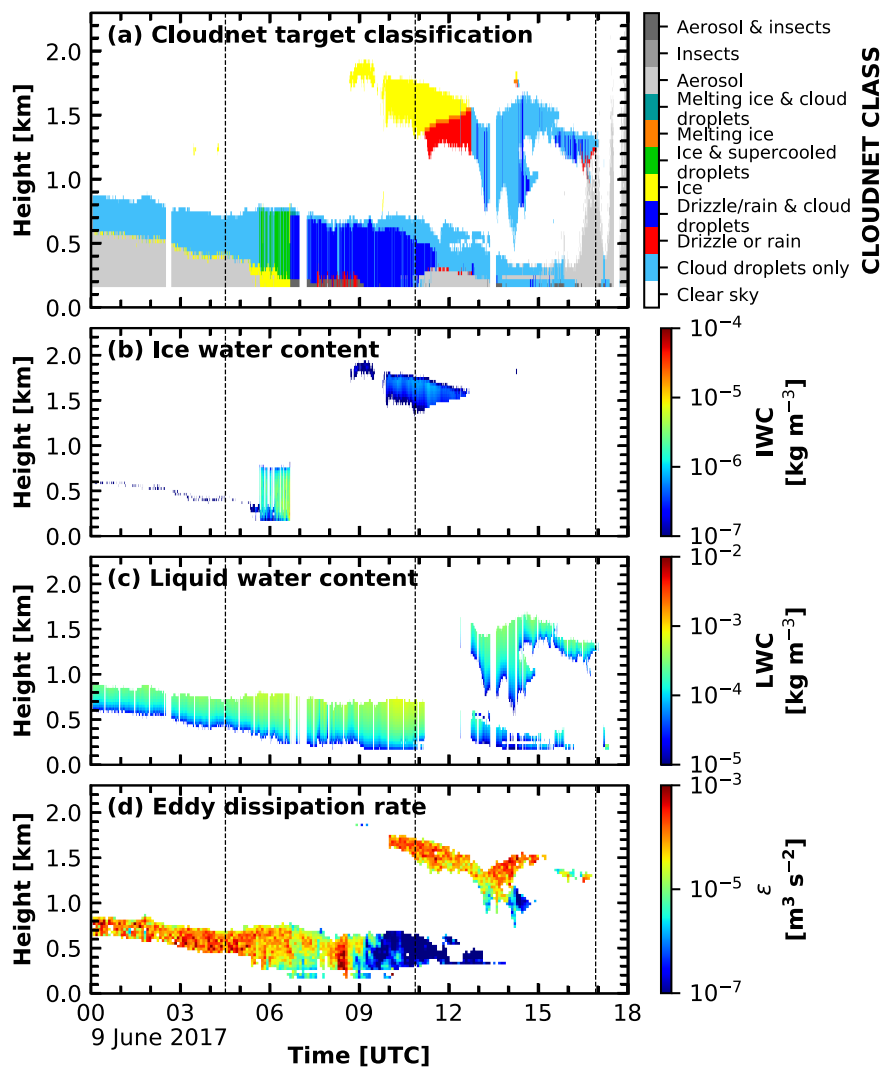
Figure 9. (a) Cloudnet target classification, (b) ice water content, and (c) liquid water content for 9 June 2017 between 00:00 – 18:00 UTC. (d) shows the time-height profile of EDR calculated from the cloud radar Doppler velocity. The dashed lines mark the time of the radiosonde launches as shown in Fig. 4.1.1.

of the surrounding radiosonde profiles reached 0 °C leading to an immediate transition from a mixed-phase to a pure liquid cloud. Therefore, no IWC and no ice effective radius were determined under these conditions.

A second transition of the cloud situation during this day is associated with an altocumulus layer which was located above the stratocumulus. Around 09:00 UTC this mid-level cloud layer with a cloud-top temperature of -1°C occurred at 1900 m
375 height over Polarstern. As this layer increased in geometrical and optical depth, shading effects reduced the cloud-top radiative cooling of the cloud below. This led to a collapse of the EDR in the lower layer at around 12:00 UTC (Fig. 9 (d)) and finally to a dissipation of the cloud. The values for ε in the altocumulus were about the same order of magnitude as for the stratocumulus, indicating that the upper cloud was able to effectively cool to space. Starting at about 14:00 UTC the altocumulus formed a two-layer structure at 1500 m and 1200 m, respectively. Due to the shading of the upper layer, the lower one lost its turbulent
380 moment and the cloud dissipated shortly after. The altocumulus was classified as pure ice cloud, probably due to the fact that the lidar signal was already fully attenuated in the lower layer which impedes the classification as liquid at an ambient temperature below 0°C. At around 11:00 UTC, the temperature exceeded 0°C, due to which Cloudnet changed its classification from an ice cloud to a liquid cloud. After persisting for about 4 hours with very low EDR, the stratocumulus started to dissipate at around 16:00 UTC. This offered the lidar the opportunity to observe the aerosol structure above Polarstern in the subsequent
385 hours (Fig. 10 (b)).

4.2 Aerosol case: 9 June 18:00 UTC – 10 June 2017 11:00 UTC, ice floe camp

Between 9 June 18:00 UTC – 10 June 2017 11:00 UTC, one of the rare cloud-free events of PS106 occurred and Polly^{XT} observed aerosol layers in the free troposphere (Fig. 10 (d)). The respective radiosonde profiles for this period are shown in Fig. 10 (a–c). Based on a Trace airmass source analysis of 27 10-day back-trajectories, a southern inflow for air masses above
390 the boundary layer is identified for this period. At the 2000 m height level, the trajectories show that these were long-range-transported aerosol layers that originated over continental Europe (Fig. 11). Below 2000 m height, the trajectories indicate that pathways mainly crossed the north sea and the Atlantic ocean.

The 1064-nm lidar attenuated backscatter coefficient and the 532-nm volume depolarization ratio are shown in Fig. 10 (d, e). These measurements reveal the existence of three aerosol layers being present over Polarstern on 9 June 2017 around
395 18:00 UTC. A shallow layer at 500 m height staying roughly at the same altitude as long it was observed by Polly^{XT}. A second one is visible between 1000 and 1500 m height ascending to 2500 m at 00:00 UTC on 10 June 2017. At 07:00 UTC on 10 June 2017, a liquid cloud formed at the top of this layer. A third aerosol layer with a liquid cloud embedded at 2300 m height, being rather constant in altitude, was present between 19:00 – 21:00 UTC on 9 June 2017.

In Figure (12), a detailed analysis of the aerosol optical properties as derived from the lidar measurements from the time
400 period of 00:00 – 02:20 UTC is presented. During this period, two layers were detected and are visible in the profiles of the backscatter coefficient at all three wavelengths (Fig. 12 (a)). The rather strong wavelength dependence of the backscatter coefficient, as shown by the high Ångstrom exponents (Fig. 12 (b)) in both layers, indicates the presence of small aerosol particles. A back-trajectory analysis and the values for the Ångstrom exponent indicates that air masses transporting polluted
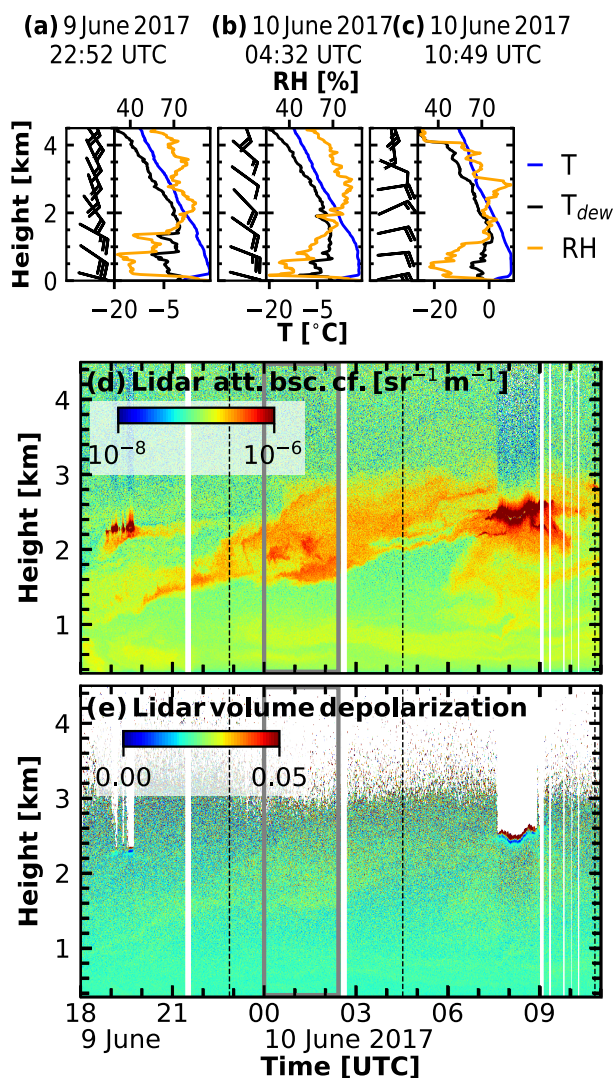
Figure 10. (a-c) same as Fig. 4.1.1 but for 9 June 2017 18:00 UTC – 10 June 2017 11:00 UTC. (d+e) measurements from Polly^{XT} between 9 June 2017, 18:00 UTC – 10 June 2017, 11:00 UTC. In (d) and (e), the 1064-nm attenuated backscatter coefficient and the 532-nm volume depolarization are shown, respectively. The black dashed lines mark the time of the radiosonde launches as shown in (a–c). The grey box indicates the period used for averaging in Fig. 12.

aerosol from continental Europe are most probably the source for the upper aerosol layer. The lower aerosol layer on the other
405 hand is most-likely a mixture of down-mixed continental and upward-mixed marine aerosol.

Based on the aerosol optical properties retrieved by Polly^{XT} an estimation of the CCNC was done for all three combinations of conversion factor and extinction exponent as mentioned in Sect. 3.4. We chose the second combination ($C_2 = 10\,\mathrm{cm}^{-3}$ and $d_2 = 0.9$) to illustrate the results in Fig. 12 (d). The mean values of CCNC for the upper aerosol layer in this case was found to
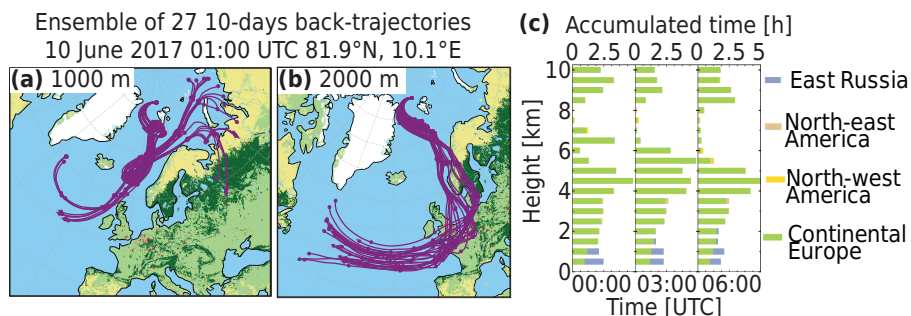
Figure 11. (a): Ensemble of 27 10-day back-trajectories arriving at the position of Polarstern at 01 UTC on 10 June 2017 in 1000 m height. (b) same as (a) but for 2000 m height. In (c) the accumulated time in hours for the ensembles above some selected areas between 00:00 – 03:00 UTC, 03:00 – 06:00 UTC and 06:00 – 09:00 UTC is shown.
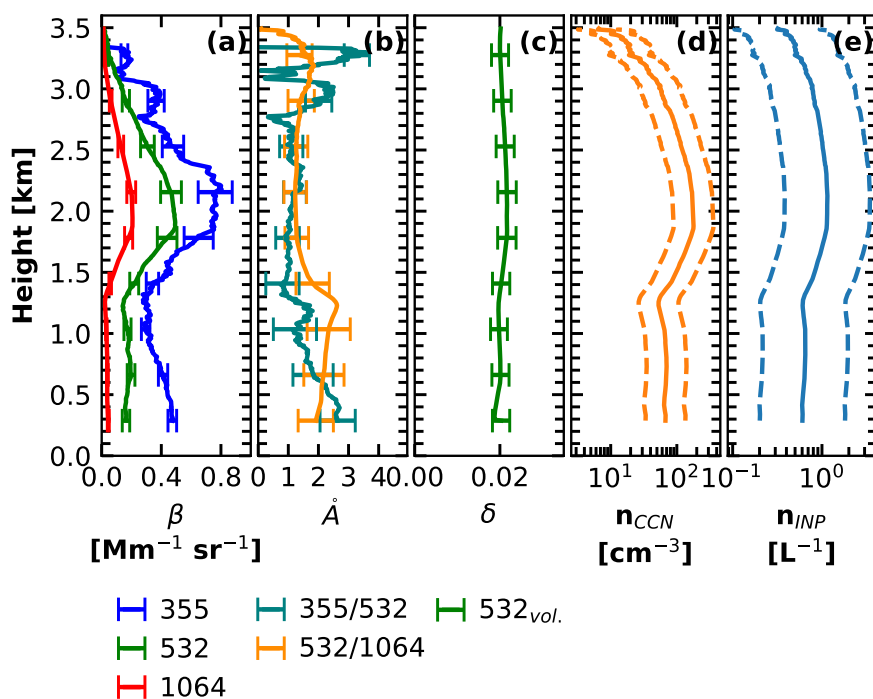
Figure 12. Averaged aerosol optical properties for the time period from 00:00 – 02:20 UTC on 10 June 2017. (a) aerosol backscatter coefficient for three wavelengths of 355 nm (blue), 532 nm (green) and 1064 nm (red). (b) Backscatter-related Ångstrom exponent for 355 nm to 532 nm (cyan) and for 532 nm to 1064 nm (orange). (c) 532-nm volume depolarization ratio. In (d) the retrieved CCN number concentration for $C_2 = 10\,\mathrm{cm}^{-3}$ and $d_2 = 0.9$ and in (e) the INP number concentration for $T = -15°C$ is shown together with the respective uncertainty (dashed lines) derived from the 532-nm backscatter coefficient profile shown in (a).
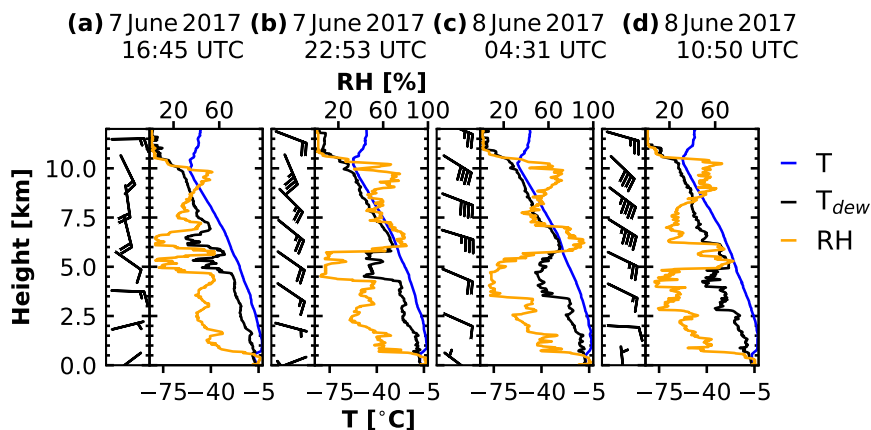
Figure 13. Same as Fig. 4.1.1 but for 7 June 2017 21:00 UTC – 8 June 2017 09:00 UTC.

be $\bar{n}_{CCN,2} = 180\,\mathrm{cm}^{-3}$. For the two other combinations, we found $\bar{n}_{CCN,1} = 260\,\mathrm{cm}^{-3}$ and $\bar{n}_{CCN,3} = 75\,\mathrm{cm}^{-3}$, respectively.

410 For the lower aerosol layer, we found $\bar{n}_{CCN,2} = 70\,\mathrm{cm}^{-3}$. For the two other combinations, we found $\bar{n}_{CCN,1} = 110\,\mathrm{cm}^{-3}$ and $\bar{n}_{CCN,3} = 25\,\mathrm{cm}^{-3}$, respectively. The uncertainty of this method is up to 200% (dashed lines in Fig. 12 (d)). In addition, the INPC was calculated for a fixed temperature of -15°C. The results are shown in Fig. 12 (e). The INPC for the lower layer was found to be around $0.6\,\mathrm{L}^{-1}$ for this temperature. In the upper layer, n_{INP} went up to values slightly above $1\,\mathrm{L}^{-1}$. These calculations have an error of 300% (dashed lines in Fig. 12 (e)) but nevertheless provide a guideline about the conditions of

415 the cloud-relevant aerosol properties on the discussed day.

4.2.1 Ice cloud: 7 June 21:00 UTC – 8 June 09:00 UTC, ice floe camp

In Figure 14, we present the OCEANET measurements for the period from 7 June, 21:00 UTC to 8 June 2017, 09:00 UTC. The corresponding thermodynamic profiles from the radiosondes launched during this time period are shown in Fig. 13. In Figure 16 (a), the Cloudnet target classification, together with the IWC (b), ice effective radius (c) and ice water path (d) are

420 shown. The ice water path is derived as the integral of the IWC for each profile. This period is chosen to illustrate the fog detection algorithm and the retrieval of the ice effective radius.

At the beginning of the addressed time period, a low-level mixed-phase stratiform cloud reaching up to a height of 500 m is present. This layer is visible in both the cloud radar reflectivity as well as in the lidar attenuated backscatter data. Due to its high optical thickness, this cloud led almost continuously until 23:30 UTC to an attenuation of the lidar signal already close to

425 cloud base (Fig. 14). Only occasionally, backscattered lidar signals from aerosols above the cloud were detected. During this period, the liquid water path varied between values of around $0\,\mathrm{g\,m}^{-2}$ for moments when the lidar was able to detect signal from above the cloud and values up to $100\,\mathrm{g\,m}^{-2}$ associated with periods when the lidar signal was attenuated already close to cloud base.
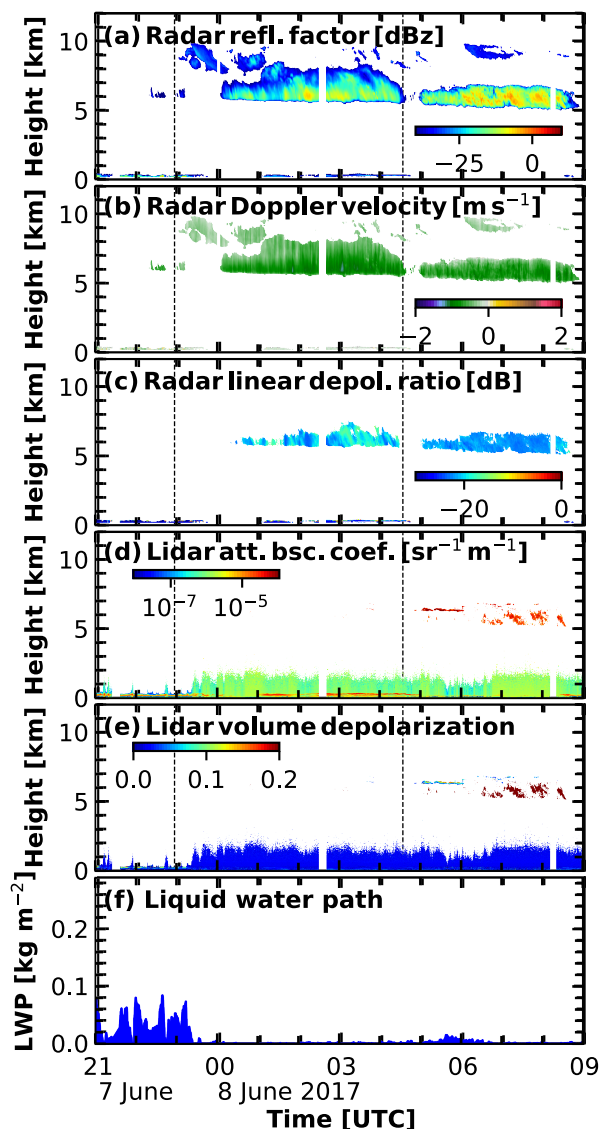
Figure 14. Same as Fig. 8 but for 7 June 2017 21:00 UTC – 8 June 2017 09:00 UTC (note: the first and last launch shown in Fig. 13 was before the plotted profiles of the measurements start).

In Figure 15, the derived fog classification mask (below 165 m height) combined with a simplified Cloudnet target classi-
430 fication mask (above 165 m height) for this period is shown. Red areas depict detected fog and low level clouds. Blue and
Green data points indicate clear sky and aerosols, respectively. Though Polly$^{\text{XT}}$ detected fog almost continuously during the
case study, this affected the lidar signal most severely during the above mentioned period. After 23:30 UTC, the LWP showed
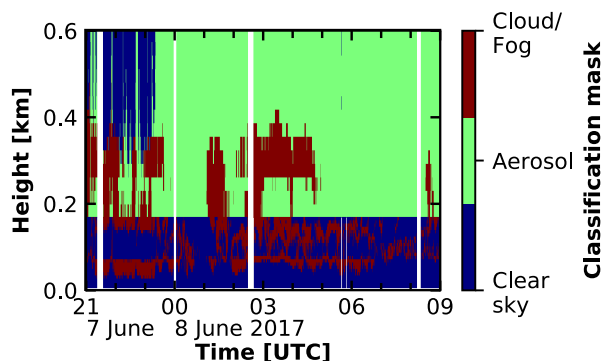
Figure 15. Fog / low-level cloud mask for 7 June 2017 21:00 UTC – 8 June 2017 09:00 UTC derived from combining Polly^{XT} and Cloudnet data. Below 165 m height, red colors indicate when fog was detected using the signal-to-noise ratio (SNR) of the Polly^{XT} 532 nm channel. Blue-shaded data points indicate when the SNR was below the fog threshold. Above 165 m height, a simplified version of the Cloudnet target classification mask is shown. Everything which was detected as cloud (either ice or liquid or mixed-phase) is masked in red. Blue depicts clear sky and green aerosols.

values of around $10 \, \mathrm{g \, m^{-2}}$ and the cloud lost most of its optical thickness so that the lidar was able to penetrate through the cloud.

435 Above the fog layer some cirrus clouds formed around 22:30 UTC above 6000 m height. These transformed into a cirrostratus layer at 00:00 UTC which was present between 6000 and 10000 m height. Until around 04:30 UTC, this cloud is classified as a pure ice cloud, characterized by LDR values of up to -15 dB and a constantly downward directed vertical velocity, with a tiny patch of detected liquid at around 03:30 UTC at 6100 m height.

At 04:30 UTC, the cirrostratus dissipated and another layer started to pass over Polarstern at around 05:00 UTC. This layer
440 with coexisting liquid droplets and ice crystals extended from 5000 m up to 7000 m height. While the cloud radar reflectivity factor was higher in this layer compared to the first one, the cloud radar LDR decreased to values of below -20 dB. On top of this layer a supercooled liquid layer was detected by the lidar between 05:00 – 06:00 UTC, characterized by high attenuated backscatter coefficient and low values of linear depolarization ratio. Additionally, some regions with high linear depolarization ratio were detected by Polly^{XT} inside the cirrus after 06:30 UTC, probably associated to a mixture of supercooled droplets and
445 ice crystals.

The IWC of the cirrostratus was found to range from $10^{-4} - 10^{-6} \, \mathrm{kg \, m^{-3}}$ with lowest values at cloud top and highest values at cloud base. The ice effective radius ranged from $30 - 55 \, \mu$m and its distribution follows the same pattern as the one of the IWC, as can be expected because both follow a similar reflectivity-temperature relationship.
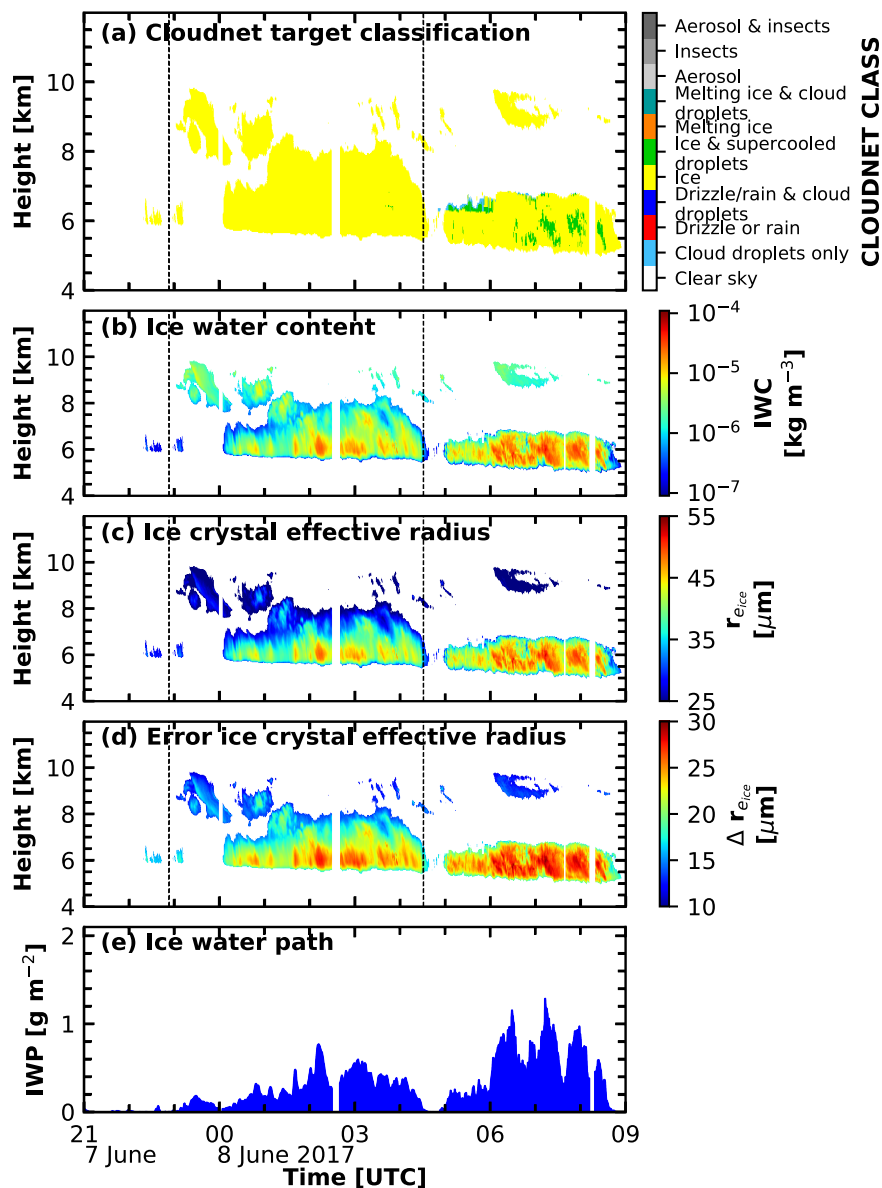
Figure 16. Cloudnet products for 7 June 2017, 21:00 UTC to 8 June 2017, 09:00 UTC: (a) target classification, (b) ice water content, (c) ice crystal effective radius, (d) uncertainty of the retrieved ice crystal effective radius as derived from error propagation, and (e) ice water path. The dashed lines mark the times of the radiosonde launches shown in Fig. 13 (note: the time of the first and last launch shown in Fig. 13 was before and after the presented time period).

4.3 Cloud statistics

450 In Figure 17, an overview about the statistical distribution of the cloud and fog occurrence during PS106 is given. In Figure 17 (a), daily statistics of the vertical distribution of fog is shown. In addition, the frequency of occurrence of fog for each day is illustrated in Fig. 17 (b). Fog was detected during a significant period of time on almost each day. The highest frequency of occurrence was observed while the Polarstern was surrounded by sea ice. Rather low values occurred while Polarstern was in the vicinity of Svalbard. Statistics of the cloud type occurrence are shown in Fig. 17 (c). The daily frequency of occurrence as

455 well as the total distribution for the complete campaign of fog (purple), liquid clouds (orange), ice clouds (light blue), mixed-phase clouds (green), multi-layer clouds (dark blue), and cloud-free situations (yellow) is shown. In addition, an analysis of the co-occurrence of fog and other cloud types was performed and is shown in the very right column of Fig. 17 (c). The rate of coexistence of the respective cloud type together with fog is indicated by a slightly varied color code.

In total, during 11% of the time cloud-free conditions were detected by Cloudnet during PS106. The two most prominent
460 cloud types were multi-layer and mixed-phase clouds with an occurrence frequency of 38.5% and 36% of the observational time, respectively. Pure ice clouds were present for about 8% and pure liquid clouds for about 4.5% of the time, respectively. Single events of the new Cloudnet class fog were detected during 2.5% of the time of the two month campaign. In addition, 27% of the observed liquid clouds and 48% of the ice clouds occurred simultaneously with fog. Mixed-phase and multi-layer clouds were detected together with fog during 24% and 27% of their respective observational time.

465 In contrast to Nomokonova et al. (2019), who provided a statistical analysis of the cloud occurrence over Ny Ålesund, Svalbard, for the period between June 2016 and July 2017, we found a higher frequency of single layer mixed-phase clouds at the expense of cloud-free and single-layer liquid clouds when comparing the period of PS106. This may be due to a difference in turbulence as well as in a change of the cloud microphysics at locations surrounded by sea ice or open ocean (Young et al., 2016).

470 ## 5 Summary and Conclusions

A two-month campaign of RV Polarstern, including an extensive suite of ground-based remote sensing instruments of the OCEANET platform, has been conducted north- and northeast of Savalbard in the Arctic summer of 2017. This study described in detail the deployed instrumentation and the applied processing schemes. Only few campaigns with a comparable equipment have been performed in recent years at these latitudes, e.g., ASCOS which took place from 2 August to 9 September 2008
475 (Tjernström et al., 2014) and ASCE in the Arctic summer and early autumn of 2014 (Tjernström et al., 2015). A new feature of PS106 was the deployment of a motion-stabilized vertically-pointing 35-GHz cloud radar during and the correction of the Doppler velocity subsequent to the cruise as specified in Sect. 3.1.

For an automatic, seamless analysis of cloud properties from the measured remote-sensing time series, the Cloudnet algorithm was utilized. In doing so, new products were developed and applied to the remote sensing data set from PS106. This was
480 done in order to enable the continuous characterization of cloud turbulence by means of EDR, and to provide mass concentration and effective radius of ice crystals and liquid water droplets as future input for radiative transfer simulations. Though
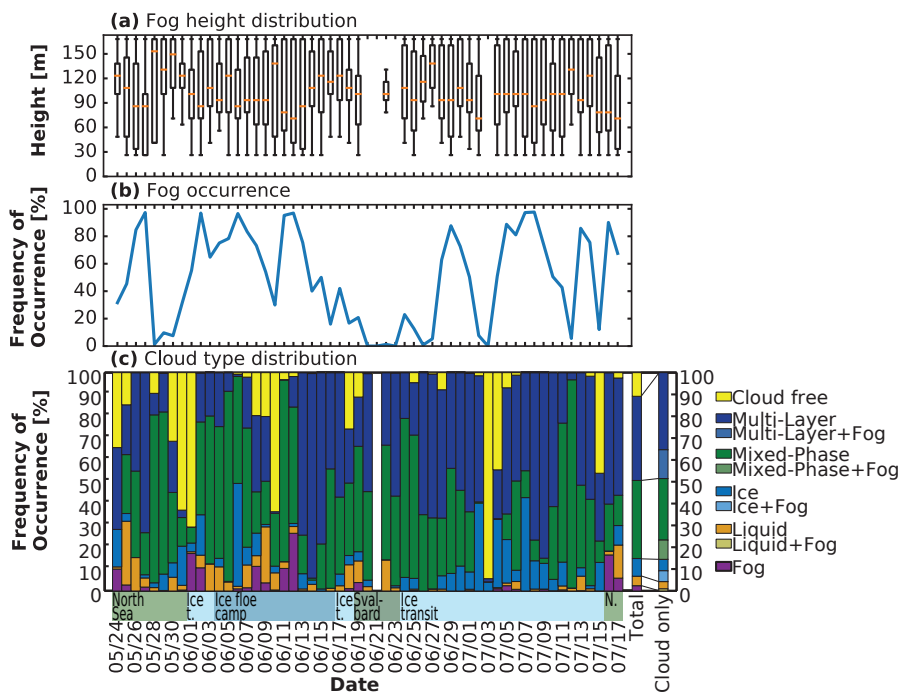
Figure 17. (a) daily height distribution of the detected fog during PS106 up to 165 m. (b) daily fraction of fog occurrence. In (c) the cloud type statistics including fog during PS106, determined by Cloudnet. Purple indicates the fraction when fog was determined, orange liquid clouds, light blue ice clouds, green mixed-phase clouds, dark blue multi-layer clouds and yellow cloud free periods. Each column except the last two represents one day of the campaign. The penultimate column represents the total distribution of the different cloud types. The last column distinguishes between the respective cloud type without fog detected (same color as in the other column) and with an additional fog layer detected below (slightly varied color). At the bottom a rough localization of Polarstern is annotated (green: North Sea (N.S.), light blue: Ice transit (Ice t.), dark blue: Ice floe camp, dark green: Svalbard region (Svalbard)).

being well established, applying the Cloudnet algorithm to data from a remote-sensing supersite aboard a research vessel in the Arctic reveals new challenges. The movement of the ship has a significant effect on the measured vertical velocity of the cloud radar. To tackle this issue, the cloud radar was mounted on a stabilization platform to guarantee its vertical pointing. The

485   vertical velocity dataset was corrected for the heave rate of the ship in a post-processing procedure subsequent to the cruise. Using the corrected vertical velocities from the cloud radar, the eddy dissipation rates were calculated. Based on published retrievals of visible extinction coefficient and ice water content, the new approach to derive the effective radius of the ice crystals was introduced. The associated uncertainties, estimated by error propagation, of the ice crystal effective radii are presented in Fig. 16 (d). On average the uncertainty is about 50% of the size of the radii themselves which reflects the strong influence of

490   uncertainties in the underlying observational data on the retrieval. Given the challenges in estimating the effective radius of ice crystals on a continuous basis on the one hand and the necessity of having such values, e.g., for radiative transfer calculations, on the other hand, we consider this estimate to be still in a reasonable range. In Figure 18, the histogram of the effective radius
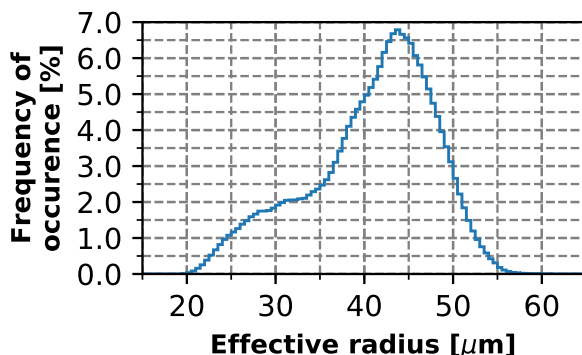
Figure 18. Histogram of the ice particle effective radius for PS106. Integration over x yields 100%.

for full PS106 is shown. Values range from $20 - 60\,\mu$m, with a peak at around $50\,\mu$m. This is consistent with other studies of ice effective radius (e.g., Blanchard et al., 2017).

495   This study revealed in addition the relevance of the lowest detection limit of remote sensing instruments on the representativity of Arctic-cloud statistics. Cloudnet is configured to have its lowest range gate at the lowest detection altitude of the cloud radar, which was 165 m above the ocean surface for PS106. Lower-level cloud layers are thus not identifiable within Cloudnet. In our study, lower cloud structures were identified using the SNR measured by the lidar Polly$^{\text{XT}}$. This ability has been used to study the occurrence of fog and low-level clouds below the first Cloudnet range gate. So far such clouds have

500   not been considered in most Arctic cloud climatologies derived by remote sensing instruments. Liu et al. (2012) for example defined low-level clouds as those between 0 and 2000 m, with 960 m above the ground being the height where surface contamination effects on Cloudsat become insignificant, and using a vertical resolution of 240 m. Shupe et al. (2011) summarized cloud statistics from several multi-year data sets derived from ground-based remote-sensing observations for different sites in the Arctic. They specified a height dependence of cloud occurrence down to 300 m by using a combination of lidar and radar.

505   Below 300 m, however, they provided information about cloud occurrence but without any further specification of the cloud base. Even airborne remote sensing instruments suffer from the strong ground clutter and thus struggle to deliver information about cloud occurrence below 150 m height above the surface (Mech et al., 2019).

    Our study shows that a higher vertical resolution and reliable signal from very low altitudes is required to characterize the lowest-level cloud layer which occur between approximately 50 m and 165 m above ground. Such clouds stay undetected

510   for ground-based in-situ sensors (because they are too high) as well as for most automated ground-based remote sensing instruments (because they are too low). Future radiative transfer studies should show what the effect of the lowest-level clouds, which occurred during 25% of the observation time, is on the radiation budget of the region where PS106 was performed.

    Future work will confront the observed cloud macro- and microphysical properties as well as the EDR with high resolution model simulations along the PS106 track that have been carried out in the framework of (AC)^3. The herein introduced remote

515   sensing techniques will also be applied to the dataset of the currently ongoing one-year polar ice drift of RV Polarstern during

the MOSAiC project (Schiermeier, 2019), thus providing an unprecedented data set of Arctic aerosol and mixed-phase clouds. This data set will substantially contribute to our understanding of the role of clouds in the current warming of the Arctic climate system.

Code and data availability. The trajectory analysis software "trace" as used for this publication is available under Radenz and Seifert (2019).
520 The most recent version is available via GitHub: https://github.com/martin-rdz/trace (last access: 04.09.2019). The radiosonde data is available by Schmithüsen (2017a) (PS106.1) and Schmithüsen (2017b) (PS106.2). The lidar measurements are available by Griesche et al. (2019d), the cloud radar measurements by Griesche et al. (2019b). The Cloudnet data set is available by Griesche et al. (2019a) and related data sets.

Acknowledgements. We gratefully acknowledge the funding by the Deutsche Forschungsgemeinschaft (DFG, German Research Foundation)
525 – Project Number 268020496 – TRR 172, within the Transregional Collaborative Research Center "ArctiC Amplification: Climate Relevant Atmospheric and SurfaCe Processes, and Feedback Mechanisms (AC)3". We thank the Alfred Wegener Institute and R/V Polarstern crew and captain for their support (AWI_PS106_00).

References

Achtert, P., Brooks, I. M., Brooks, B. J., Moat, B. I., Prytherch, J., Persson, P. O. G., and Tjernström, M.: Measurement of wind profiles by
530   motion-stabilised ship-borne Doppler lidar, Atmospheric Measurement Techniques, 8, 4993–5007, https://doi.org/10.5194/amt-8-4993-
       2015, https://www.atmos-meas-tech.net/8/4993/2015/, 2015.

Anderson, G., Clough, S., Kneizys, F., Chetwynd, J., and Shettle, E.: AFGL atmospheric constituent profiles (0–120 km), techreport, AIR
       FORCE GEOPHYSICS LAB HANSCOM AFB MA, https://apps.dtic.mil/dtic/tr/fulltext/u2/a175173.pdf, 1986.

Baars, H., Ansmann, A., Althausen, D., Engelmann, R., Artaxo, P., Pauliquevis, T., and Souza, R.: Further evidence for significant
535   smoke transport from Africa to Amazonia, Geophysical Research Letters, 38, https://doi.org/10.1029/2011GL049200, https://agupubs.
       onlinelibrary.wiley.com/doi/abs/10.1029/2011GL049200, 2011.

Baars, H., Ansmann, A., Althausen, D., Engelmann, R., Heese, B., Müller, D., Artaxo, P., Paixao, M., Pauliquevis, T., and Souza, R.:
       Aerosol profiling with lidar in the Amazon Basin during the wet and dry season, Journal of Geophysical Research: Atmospheres, 117,
       https://doi.org/10.1029/2012JD018338, https://agupubs.onlinelibrary.wiley.com/doi/abs/10.1029/2012JD018338, 2012.

540 Baars, H., Seifert, P., Engelmann, R., and Wandinger, U.: Target categorization of aerosol and clouds by continuous multiwavelength-
       polarization lidar measurements, Atmospheric Measurement Techniques, 10, 3175–3201, https://doi.org/10.5194/amt-10-3175-2017,
       https://www.atmos-meas-tech.net/10/3175/2017/, 2017.

Barrientos Velasco, C., Deneke, H., Griesche, H., Seifert, P., Engelmann, R., and Macke, A.: Spatiotemporal variability of shortwave radiation
       introduced by clouds over the Arctic sea ice, Atmospheric Measurement Techniques Discussions, 2019, 1–36, https://doi.org/10.5194/amt-
545   2019-231, https://www.atmos-meas-tech-discuss.net/amt-2019-231/, 2019.

Bühl, J., Ansmann, A., Seifert, P., Baars, H., and Engelmann, R.: Toward a quantitative characterization of heterogeneous ice for-
       mation with lidar/radar: Comparison of CALIPSO/CloudSat with ground-based observations, Geophys. Res. Lett., 40, 4404–4408,
       https://doi.org/10.1002/grl.50792, https://doi.org/10.1002/grl.50792, 2013.

Blanchard, Y., Royer, A., O'Neill, N. T., Turner, D. D., and Eloranta, E. W.: Thin ice clouds in the Arctic: cloud optical depth
550   and particle size retrieved from ground-based thermal infrared radiometry, Atmospheric Measurement Techniques, 10, 2129–2147,
       https://doi.org/10.5194/amt-10-2129-2017, https://www.atmos-meas-tech.net/10/2129/2017/, 2017.

Borque, P., Luke, E., and Kollias, P.: On the unified estimation of turbulence eddy dissipation rate using Doppler cloud radars and lidars,
       Journal of Geophysical Research: Atmospheres, 121, 5972–5989, https://doi.org/10.1002/2015JD024543, https://agupubs.onlinelibrary.
       wiley.com/doi/abs/10.1002/2015JD024543, 2016.

555 Bühl, J., Seifert, P., Myagkov, A., and Ansmann, A.: Measuring ice- and liquid-water properties in mixed-phase cloud layers at the
       Leipzig Cloudnet station, Atmospheric Chemistry and Physics, 16, 10 609–10 620, https://doi.org/10.5194/acp-16-10609-2016, https:
       //www.atmos-chem-phys.net/16/10609/2016/, 2016.

Caughey, S. J., Wyngaard, J. C., and Kaimal, J. C.: Turbulence in the Evolving Stable Boundary Layer, Journal of the Atmospheric Sciences,
       36, 1041–1052, 1979.

560 Curry, J. A., Hobbs, P. V., King, M. D., Randall, D. A., Minnis, P., Isaac, G. A., Pinto, J. O., Uttal, T., Bucholtz, A., Cripe, D. G., Gerber,
       H., Fairall, C. W., Garrett, T. J., Hudson, J., Intrieri, J. M., Jakob, C., Jensen, T., Lawson, P., Marcotte, D., Nguyen, L., Pilewskie,
       P., Rangno, A., Rogers, D. C., Strawbridge, K. B., Valero, F. P. J., Williams, A. G., and Wylie, D.: FIRE Arctic Clouds Experiment,
       Bulletin of the American Meteorological Society, 81, 5–30, https://doi.org/10.1175/1520-0477(2000)081<0005:FACE>2.3.CO;2, https:
       //doi.org/10.1175/1520-0477(2000)081<0005:FACE>2.3.CO;2, 2000.

565 Dai, G., Althausen, D., Hofer, J., Engelmann, R., Seifert, P., Bühl, J., Mamouri, R.-E., Wu, S., and Ansmann, A.: Calibration of Raman
lidar water vapor profiles by means of AERONET photometer observations and GDAS meteorological data, Atmospheric Measurement
Techniques, 11, 2735–2748, https://doi.org/10.5194/amt-11-2735-2018, https://www.atmos-meas-tech.net/11/2735/2018/, 2018.

de Boer, G., Eloranta, E. W., and Shupe, M. D.: Arctic Mixed-Phase Stratiform Cloud Properties from Multiple Years of Surface-Based Mea-
surements at Two High-Latitude Locations, Journal of the Atmospheric Sciences, 66, 2874–2887, https://doi.org/10.1175/2009JAS3029.1,
570 https://doi.org/10.1175/2009JAS3029.1, 2009.

Delanoë, J., Protat, A., Bouniol, D., Heymsfield, A., Bansemer, A., and Brown, P.: The Characterization of Ice Cloud Properties from
Doppler Radar Measurements, Journal of Applied Meteorology and Climatology, 46, 1682–1698, https://doi.org/10.1175/JAM2543.1,
https://doi.org/10.1175/JAM2543.1, 2007.

DeMott, P. J., Prenni, A. J., Liu, X., Kreidenweis, S. M., Petters, M. D., Twohy, C. H., Richardson, M. S., Eidhammer, T., and Rogers, D. C.:
575 Predicting global atmospheric ice nuclei distributions and their impacts on climate, Proceedings of the National Academy of Sciences,
107, 11 217–11 222, https://doi.org/10.1073/pnas.0910818107, https://www.pnas.org/content/107/25/11217, 2010.

Ebell, K., Maturilli, M., Nomokonova, T., and Ritter, C.: Radiative effect of clouds at Ny-Ålesund, Svalbard, as inferred from ground-based
remote sensing observations, submitted to Journal of Applied Meteorology and Climatology, 2019.

Egerer, U., Gottschalk, M., Siebert, H., Ehrlich, A., and Wendisch, M.: The new BELUGA setup for collocated turbulence and radiation
580 measurements using a tethered balloon: first applications in the cloudy Arctic boundary layer, Atmospheric Measurement Techniques, 12,
4019–4038, https://doi.org/10.5194/amt-12-4019-2019, https://www.atmos-meas-tech.net/12/4019/2019/, 2019.

Engelmann, R., Kanitz, T., Baars, H., Heese, B., Althausen, D., Skupin, A., Wandinger, U., Komppula, M., Stachlewska, I. S., Amiridis,
V., Marinou, E., Mattis, I., Linné, H., and Ansmann, A.: The automated multiwavelength Raman polarization and water-vapor lidar
Polly^{XT}: the neXT generation, Atmospheric Measurement Techniques, 9, 1767–1784, https://doi.org/10.5194/amt-9-1767-2016, https:
585 //www.atmos-meas-tech.net/9/1767/2016/, 2016.

Foth, A., Kanitz, T., Engelmann, R., Baars, H., Radenz, M., Seifert, P., Barja, B., Fromm, M., Kalesse, H., and Ansmann, A.: Vertical aerosol
distribution in the southern hemispheric midlatitudes as observed with lidar in Punta Arenas, Chile ($53.2°$ S and $70.9°$ W), during AL-
PACA, Atmospheric Chemistry and Physics, 19, 6217–6233, https://doi.org/10.5194/acp-19-6217-2019, https://www.atmos-chem-phys.
net/19/6217/2019/, 2019.

590 Frehlich, R. and Cornman, L.: Estimating Spatial Velocity Statistics with Coherent Doppler Lidar, Journal of Atmospheric and Oceanic
Technology, 19, 355–366, https://doi.org/10.1175/1520-0426-19.3.355, https://doi.org/10.1175/1520-0426-19.3.355, 2002.

Frisch, A. S., Feingold, G., Fairall, C. W., Uttal, T., and Snider, J. B.: On cloud radar and microwave radiometer measurements of stratus cloud
liquid water profiles, Journal of Geophysical Research: Atmospheres, 103, 23 195–23 197, https://doi.org/10.1029/98JD01827, https://
agupubs.onlinelibrary.wiley.com/doi/abs/10.1029/98JD01827, 1998.

595 Frisch, S., Shupe, M., Djalalova, I., Feingold, G., and Poellot, M.: The Retrieval of Stratus Cloud Droplet Effective Radius with Cloud Radars,
Journal of Atmospheric and Oceanic Technology, 19, 835–842, https://doi.org/10.1175/1520-0426(2002)019<0835:TROSCD>2.0.CO;2,
https://doi.org/10.1175/1520-0426(2002)019<0835:TROSCD>2.0.CO;2, 2002.

GDAS: Global Data Assimilation System, Tech. rep., NOAA, https://www.ncdc.noaa.gov/data-access/model-data/model-datasets/
global-data-assimilation-system-gdas.

600 Goosse, H., Kay, J. E., Armour, K. C., Bodas-Salcedo, A., Chepfer, H., Docquier, D., Jonko, A., Kushner, P. J., Lecomte, O., Massonnet, F.,
Park, H.-S., Pithan, F., Svensson, G., and Vancoppenolle, M.: Quantifying climate feedbacks in polar regions, Nature Communications, 9,
1919, https://doi.org/10.1038/s41467-018-04173-0, 2018.

Görsdorf, U., Lehmann, V., Bauer-Pfundstein, M., Peters, G., Vavriv, D., Vinogradov, V., and Volkov, V.: A 35-GHz Polarimetric Doppler Radar for Long-Term Observations of Cloud Parameters—Description of System and Data Processing, Journal of Atmospheric and
605   Oceanic Technology, 32, 675–690, https://doi.org/10.1175/JTECH-D-14-00066.1, https://doi.org/10.1175/JTECH-D-14-00066.1, 2015.

Granskog, M. A., Fer, I., Rinke, A., and Steen, H.: Atmosphere-Ice-Ocean-Ecosystem Processes in a Thinner Arctic Sea Ice Regime: The Norwegian Young Sea ICE (N-ICE2015) Expedition, J. Geophys. Res. Oceans, 123, 1586–1594, https://doi.org/10.1002/2017jc013328, https://doi.org/10.1002/2017JC013328, 2018.

Griesche, H., Seifert, P., Engelmann, R., Radenz, M., and Bühl, J.: Cloudnet target classification during POLARSTERN cruise PS106
610   classification, https://doi.org/10.1594/PANGAEA.900245, https://doi.org/10.1594/PANGAEA.900245, 2019a.

Griesche, H., Seifert, P., Engelmann, R., Radenz, M., and Bühl, J.: OCEANET Cloud radar Mira-35 during POLARSTERN cruise PS106, https://doi.org/10.1594/PANGAEA.899895, https://doi.org/10.1594/PANGAEA.899895, 2019b.

Griesche, H., Seifert, P., Engelmann, R., Radenz, M., and Bühl, J.: OCEANET-ATMOSPHERE Mircowave Radiometer Hatpro during POLARSTERN cruise PS106, https://doi.org/10.1594/PANGAEA.899898, https://doi.org/10.1594/PANGAEA.899898, 2019c.

615   Griesche, H., Seifert, P., Engelmann, R., Radenz, M., and Bühl, J.: OCEANET-ATMOSPHERE PollyXT measurements during PO-LARSTERN cruise PS106, https://doi.org/10.1594/PANGAEA.899458, https://doi.org/10.1594/PANGAEA.899458, 2019d.

Heese, B., Flentje, H., Althausen, D., Ansmann, A., and Frey, S.: Ceilometer lidar comparison: backscatter coefficient retrieval and signal-to-noise ratio determination, Atmospheric Measurement Techniques, 3, 1763–1770, https://doi.org/10.5194/amt-3-1763-2010, https://www.atmos-meas-tech.net/3/1763/2010/, 2010.

620   Hogan, R. and O'Connor, E.: Facilitating cloud radar and lidar algorithms: the Cloudnet Instrument Synergy / Target Categorization product, Tech. rep., http://www.met.rdg.ac.uk/~swrhgnrj/publications/categorization.pdf, 2004.

Hogan, R. J., Mittermaier, M. P., and Illingworth, A. J.: The Retrieval of Ice Water Content from Radar Reflectivity Factor and Temperature and Its Use in Evaluating a Mesoscale Model, Journal of Applied Meteorology and Climatology, 45, 301–317, https://doi.org/10.1175/JAM2340.1, https://doi.org/10.1175/JAM2340.1, 2006.

625   Iacono, M. J., Delamere, J. S., Mlawer, E. J., Shephard, M. W., Clough, S. A., and Collins, W. D.: Radiative forcing by long-lived greenhouse gases: Calculations with the AER radiative transfer models, Journal of Geophysical Research: Atmospheres, 113, https://doi.org/10.1029/2008JD009944, https://agupubs.onlinelibrary.wiley.com/doi/abs/10.1029/2008JD009944, 2008.

Illingworth, A. J., Hogan, R. J., O'Connor, E., Bouniol, D., Brooks, M. E., Delanoé, J., Donovan, D. P., Eastment, J. D., Gaussiat, N., Goddard, J. W. F., Haeffelin, M., Baltink, H. K., Krasnov, O. A., Pelon, J., Piriou, J.-M., Protat, A., Russchenberg, H. W. J., Seifert,
630   A., Tompkins, A. M., van Zadelhoff, G.-J., Vinit, F., Willén, U., Wilson, D. R., and Wrench, C. L.: Cloudnet, Bulletin of the American Meteorological Society, 88, 883–898, https://doi.org/10.1175/BAMS-88-6-883, https://doi.org/10.1175/BAMS-88-6-883, 2007.

Jacob, D. J., Crawford, J. H., Maring, H., Clarke, A. D., Dibb, J. E., Emmons, L. K., Ferrare, R. A., Hostetler, C. A., Russell, P. B., Singh, H. B., Thompson, A. M., Shaw, G. E., McCauley, E., Pederson, J. R., and Fisher, J. A.: The Arctic Research of the Composition of the Troposphere from Aircraft and Satellites (ARCTAS) mission: design, execution, and first results, Atmospheric Chemistry and Physics,
635   10, 5191–5212, https://doi.org/10.5194/acp-10-5191-2010, https://www.atmos-chem-phys.net/10/5191/2010/, 2010.

Kaimal, J. C., Wyngaard, J. C., Haugen, D. A., Coté, O. R., Izumi, Y., Caughey, S. J., and Readings, C. J.: Turbulence Structure in the Convective Boundary Layer, Journal of the Atmospheric Sciences, 33, 2152–2169, https://doi.org/10.1175/1520-0469(1976)033<2152:TSITCB>2.0.CO;2, https://doi.org/10.1175/1520-0469(1976)033<2152:TSITCB>2.0.CO;2, 1976.

Kalesse, H. and Kollias, P.: Climatology of High Cloud Dynamics Using Profiling ARM Doppler Radar Observations, Journal of Climate,
640   26, 6340–6359, https://doi.org/10.1175/JCLI-D-12-00695.1, https://doi.org/10.1175/JCLI-D-12-00695.1, 2013.

Kalesse, H., de Boer, G., Solomon, A., Oue, M., Ahlgrimm, M., Zhang, D., Shupe, M. D., Luke, E., and Protat, A.: Understanding Rapid Changes in Phase Partitioning between Cloud Liquid and Ice in Stratiform Mixed-Phase Clouds: An Arctic Case Study, Monthly Weather Review, 144, 4805–4826, https://doi.org/10.1175/MWR-D-16-0155.1, https://doi.org/10.1175/MWR-D-16-0155.1, 2016a.

Kalesse, H., Szyrmer, W., Kneifel, S., Kollias, P., and Luke, E.: Fingerprints of a riming event on cloud radar Doppler spectra: obser-
645   vations and modeling, Atmospheric Chemistry and Physics, 16, 2997–3012, https://doi.org/10.5194/acp-16-2997-2016, https://www. atmos-chem-phys.net/16/2997/2016/, 2016b.

Kanitz, T., Ansmann, A., Engelmann, R., and Althausen, D.: North-south cross sections of the vertical aerosol distribution over the Atlantic Ocean from multiwavelength Raman/polarization lidar during Polarstern cruises, Journal of Geophysical Research: Atmospheres, 118, 2643–2655, https://doi.org/10.1002/jgrd.50273, https://agupubs.onlinelibrary.wiley.com/doi/abs/10.1002/jgrd.50273, 2013a.

650   Kanitz, T., Ansmann, A., Seifert, P., Engelmann, R., Kalisch, J., and Althausen, D.: Radiative effect of aerosols above the northern and southern Atlantic Ocean as determined from shipborne lidar observations, Journal of Geophysical Research: Atmospheres, 118, 12,556– 12,565, https://doi.org/10.1002/2013JD019750, https://agupubs.onlinelibrary.wiley.com/doi/abs/10.1002/2013JD019750, 2013b.

Kecorius, S., Vogl, T., Paasonen, P., Lampilahti, J., Rothenberg, D., Wex, H., Zeppenfeld, S., van Pinxteren, M., Hartmann, M., Henning, S., Gong, X., Welti, A., Kulmala, M., Stratmann, F., Herrmann, H., and Wiedensohler, A.: New particle formation and its effect on
655   CCN abundance in the summer Arctic: a case study during PS106 cruise, Atmospheric Chemistry and Physics Discussions, 2019, 1–41, https://doi.org/10.5194/acp-2019-600, https://www.atmos-chem-phys-discuss.net/acp-2019-600/, 2019.

Klepp, C., Michel, S., Protat, A., Burdanowitz, J., Albern, N., Kahnert, M., Dahl, A., Louf, V., Bakan, S., and Buehler, S. A.: OceanRAIN, a new in-situ shipboard global ocean surface-reference dataset of all water cycle components, Sci Data, 5, 180 122, https://doi.org/10.1038/sdata.2018.122, 2018.

660   Löhnert, U. and Crewell, S.: Accuracy of cloud liquid water path from ground-based microwave radiometry 1. Dependency on cloud model statistics, Radio Science, 38, https://doi.org/10.1029/2002RS002654, https://agupubs.onlinelibrary.wiley.com/doi/abs/10.1029/ 2002RS002654, 2003.

Liu, Y., Key, J. R., Ackerman, S. A., Mace, G. G., and Zhang, Q.: Arctic cloud macrophysical characteristics from CloudSat and CALIPSO, Remote Sensing of Environment, 124, 159 – 173, https://doi.org/10.1016/j.rse.2012.05.006, http://www.sciencedirect.com/science/article/
665   pii/S003442571200209X, 2012.

Lothon, M., Lenschow, D. H., Leon, D., and Vali, G.: Turbulence measurements in marine stratocumulus with airborne Doppler radar, Quarterly Journal of the Royal Meteorological Society, 131, 2063–2080, https://doi.org/10.1256/qj.04.131, https://rmets.onlinelibrary. wiley.com/doi/abs/10.1256/qj.04.131, 2005.

Macke, A. and Flores, H.: The Expeditions PS106/1 and 2 of the Research Vessel POLARSTERN to the Arctic Ocean in 2017,
670   https://doi.org/10.2312/BzPM_0719_2018, 2018.

Mamouri, R.-E. and Ansmann, A.: Potential of polarization lidar to provide profiles of CCN- and INP-relevant aerosol parameters, Atmospheric Chemistry and Physics, 16, 5905–5931, https://doi.org/10.5194/acp-16-5905-2016, https://www.atmos-chem-phys.net/16/5905/ 2016/, 2016.

Maturilli, M.: High resolution radiosonde measurements from station Ny-Ålesund (2017-06), https://doi.org/10.1594/PANGAEA.879822,
675   https://doi.org/10.1594/PANGAEA.879822, 2017.

McFarquhar, G. M., Ghan, S., Verlinde, J., Korolev, A., Strapp, J. W., Schmid, B., Tomlinson, J. M., Wolde, M., Brooks, S. D., Cziczo, D., Dubey, M. K., Fan, J., Flynn, C., Gultepe, I., Hubbe, J., Gilles, M. K., Laskin, A., Lawson, P., Leaitch, W. R., Liu, P., Liu, X., Lubin, D., Mazzoleni, C., Macdonald, A.-M., Moffet, R. C., Morrison, H., Ovchinnikov, M., Shupe, M. D., Turner, D. D., Xie, S., Zelenyuk, A., Bae,

K., Freer, M., and Glen, A.: Indirect and Semi-direct Aerosol Campaign, Bulletin of the American Meteorological Society, 92, 183–201,
https://doi.org/10.1175/2010BAMS2935.1, https://doi.org/10.1175/2010BAMS2935.1, 2011.

Mech, M., Kliesch, L.-L., Anhäuser, A., Rose, T., Kollias, P., and Crewell, S.: Microwave Radar/radiometer for Arctic Clouds (MiRAC):
first insights from the ACLOUD campaign, Atmospheric Measurement Techniques, 12, 5019–5037, https://doi.org/10.5194/amt-12-5019-
2019, 2019.

Meier, W. N., Hovelsrud, G. K., van Oort, B. E. H., Key, J. R., Kovacs, K. M., Michel, C., Haas, C., Granskog, M. A., Gerland, S., Perovich,
D. K., Makshtas, A., and Reist, J. D.: Arctic sea ice in transformation: A review of recent observed changes and impacts on biology and
human activity, Rev. Geophys., 52, 185–217, https://doi.org/10.1002/2013rg000431, https://doi.org/10.1002/2013RG000431, 2014.

Meischner, P., Baumann, R., Höller, H., and Jank, T.: Eddy Dissipation Rates in Thunderstorms Estimated by Doppler Radar in Rela-
tion to Aircraft In Situ Measurements, Journal of Atmospheric and Oceanic Technology, 18, 1609–1627, https://doi.org/10.1175/1520-
0426(2001)018<1609:EDRITE>2.0.CO;2, https://doi.org/10.1175/1520-0426(2001)018<1609:EDRITE>2.0.CO;2, 2001.

Merk, D., Deneke, H., Pospichal, B., and Seifert, P.: Investigation of the adiabatic assumption for estimating cloud micro- and macrophysical
properties from satellite and ground observations, Atmospheric Chemistry and Physics, 16, 933–952, https://doi.org/10.5194/acp-16-933-
2016, https://www.atmos-chem-phys.net/16/933/2016/, 2016.

Miles, N. L., Verlinde, J., and Clothiaux, E. E.: Cloud Droplet Size Distributions in Low-Level Stratiform Clouds., Journal of Atmospheric
Sciences, 57, 295–311, https://doi.org/10.1175/1520-0469(2000)057<0295:CDSDIL>2.0.CO;2, 2000.

Müller, D., Ansmann, A., Mattis, I., Tesche, M., Wandinger, U., Althausen, D., and Pisani, G.: Aerosol-type-dependent lidar ratios ob-
served with Raman lidar, Journal of Geophysical Research: Atmospheres, 112, https://doi.org/10.1029/2006JD008292, https://agupubs.
onlinelibrary.wiley.com/doi/abs/10.1029/2006JD008292, 2007.

Morrison, H., de Boer, G., Feingold, G., Harrington, J., Shupe, M. D., and Sulia, K.: Resilience of persistent Arctic mixed-phase clouds,
Nature Geoscience, 5, 11–17, https://doi.org/10.1038/ngeo1332, 2012.

Müller, D., Wandinger, U., and Ansmann, A.: Microphysical particle parameters from extinction and backscatter lidar data by inver-
sion with regularization: theory, Appl. Opt., 38, 2346–2357, https://doi.org/10.1364/AO.38.002346, http://ao.osa.org/abstract.cfm?URI=
ao-38-12-2346, 1999.

Neggers, R. e. a.: Local and remote controls on Arctic mixed-layer evolution (in submitted to JAMES), Journal of Advances in Modeling
Earth Systems, 2019.

Nicholls, S.: Measurements of turbulence by an instrumented aircraft in a convective atmospheric boundary layer over the sea, Quarterly
Journal of the Royal Meteorological Society, 104, 653–676, https://doi.org/10.1002/qj.49710444109, https://rmets.onlinelibrary.wiley.
com/doi/abs/10.1002/qj.49710444109, 1978.

Nomokonova, T., Ebell, K., Löhnert, U., Maturilli, M., Ritter, C., and O'Connor, E.: Statistics on clouds and their relation to ther-
modynamic conditions at Ny-Ålesund using ground-based sensor synergy, Atmospheric Chemistry and Physics, 19, 4105–4126,
https://doi.org/10.5194/acp-19-4105-2019, https://www.atmos-chem-phys.net/19/4105/2019/, 2019.

Nucciarone, J. J. and Young, G. S.: Aircraft Measurements of Turbulence Spectra in the Marine Stratocumulus-topped Boundary Layer,
Journal of the Atmospheric Sciences, 48, 2382–2392, https://doi.org/10.1175/1520-0469(1991)048<2382:AMOTSI>2.0.CO;2, https://
doi.org/10.1175/1520-0469(1991)048<2382:AMOTSI>2.0.CO;2, 1991.

O'Connor, E. J., Illingworth, A. J., Brooks, I. M., Westbrook, C. D., Hogan, R. J., Davies, F., and Brooks, B. J.: A Method for Estimating
the Turbulent Kinetic Energy Dissipation Rate from a Vertically Pointing Doppler Lidar, and Independent Evaluation from Balloon-Borne

In Situ Measurements, Journal of Atmospheric and Oceanic Technology, 27, 1652–1664, https://doi.org/10.1175/2010JTECHA1455.1, https://doi.org/10.1175/2010JTECHA1455.1, 2010.

Pithan, F. and Mauritsen, T.: Arctic amplification dominated by temperature feedbacks in contemporary climate models, Nature Geoscience, 7, 181, https://doi.org/10.1038/ngeo2071, 2014.

720 Radenz, M. and Seifert, P.: Software for automated trajectory analysis: trace, https://doi.org/10.5281/zenodo.2576559, https://doi.org/10.5281/zenodo.2576559, 2019.

Radenz, M., Bühl, J., Seifert, P., Griesche, H., and Engelmann, R.: peakTree: a framework for structure-preserving radar Doppler spectra analysis, Atmospheric Measurement Techniques, 12, 4813–4828, https://doi.org/10.5194/amt-12-4813-2019, https://www.atmos-meas-tech.net/12/4813/2019/, 2019.

725 Rose, T., Crewell, S., Löhnert, U., and Simmer, C.: A network suitable microwave radiometer for operational monitoring of the cloudy atmosphere, Atmospheric Research, 75, 183 – 200, https://doi.org/https://doi.org/10.1016/j.atmosres.2004.12.005, http://www.sciencedirect.com/science/article/pii/S0169809505000189, cLIWA-NET: Observation and Modelling of Liquid Water Clouds, 2005.

Sathe, A. and Mann, J.: A review of turbulence measurements using ground-based wind lidars, Atmospheric Measurement Techniques, 6, 3147–3167, https://doi.org/10.5194/amt-6-3147-2013, https://www.atmos-meas-tech.net/6/3147/2013/, 2013.

730 Schiermeier, Q.: Trapped: why 300 scientists are locking themselves in Arctic ice, Nature News Article, https://doi.org/10.1038/d41586-019-02823-x, 2019.

Schmithüsen, H.: Upper air soundings during POLARSTERN cruise PS106/1 (ARK-XXXI/1.1), https://doi.org/10.1594/PANGAEA.882736, https://doi.org/10.1594/PANGAEA.882736, 2017a.

Schmithüsen, H.: Upper air soundings during POLARSTERN cruise PS106/2 (ARK-XXXI/1.2), 735 https://doi.org/10.1594/PANGAEA.882843, https://doi.org/10.1594/PANGAEA.882843, 2017b.

Seifert, P., Ansmann, A., Mattis, I., Wandinger, U., Tesche, M., Engelmann, R., Müller, D., Pérez, C., and Haustein, K.: Saharan dust and heterogeneous ice formation: Eleven years of cloud observations at a central European EARLINET site, J. Geophys. Res., 115, https://doi.org/10.1029/2009jd013222, https://doi.org/10.1029/2009JD013222, 2010.

Seifert, P., Kunz, C., Baars, H., Ansmann, A., Bühl, J., Senf, F., Engelmann, R., Althausen, D., and Artaxo, P.: Seasonal variability 740 of heterogeneous ice formation in stratiform clouds over the Amazon Basin, Geophysical Research Letters, 42, 5587–5593, https://doi.org/10.1002/2015GL064068, https://agupubs.onlinelibrary.wiley.com/doi/abs/10.1002/2015GL064068, 2015.

Serreze, M. C. and Barry, R. G.: Processes and impacts of Arctic amplification: A research synthesis, Global and Planetary Change, 77, 85 – 96, http://www.sciencedirect.com/science/article/pii/S0921818111000397, 2011.

Shupe, M. D., Kollias, P., Matrosov, S. Y., and Schneider, T. L.: Deriving Mixed-Phase Cloud Properties from Doppler Radar Spectra, 745 Journal of Atmospheric and Oceanic Technology, 21, 660–670, https://doi.org/10.1175/1520-0426(2004)021<0660:DMCPFD>2.0.CO;2, https://doi.org/10.1175/1520-0426(2004)021<0660:DMCPFD>2.0.CO;2, 2004.

Shupe, M. D., Walden, V. P., Eloranta, E., Uttal, T., Campbell, J. R., Starkweather, S. M., and Shiobara, M.: Clouds at Arctic Atmospheric Observatories. Part I: Occurrence and Macrophysical Properties, Journal of Applied Meteorology and Climatology, 50, 626–644, http://www.jstor.org/stable/26174047, 2011.

750 Shupe, M. D., Brooks, I. M., and Canut, G.: Evaluation of turbulent dissipation rate retrievals from Doppler Cloud Radar, Atmospheric Measurement Techniques, 5, 1375–1385, https://doi.org/10.5194/amt-5-1375-2012, https://www.atmos-meas-tech.net/5/1375/2012/, 2012.

Shupe, M. D., Persson, P. O. G., Brooks, I. M., Tjernstrom, M., Sedlar, J., Mauritsen, T., Sjogren, S., and Leck, C.: Cloud and boundary layer interactions over the Arctic sea ice in late summer, Atmospheric Chemistry and Physics, 13, 9379–9399, https://doi.org/10.5194/acp-13-9379-2013, 2013.

755 Siebert, H., Franke, H., Lehmann, K., Maser, R., Saw, E. W., Schell, D., Shaw, R. A., and Wendisch, M.: Probing Finescale Dynamics and Microphysics of Clouds with Helicopter-Borne Measurements, Bulletin of the American Meteorological Society, 87, 1727–1738, https://doi.org/10.1175/BAMS-87-12-1727, https://doi.org/10.1175/BAMS-87-12-1727, 2006a.

Siebert, H., Lehmann, K., and Wendisch, M.: Observations of Small-Scale Turbulence and Energy Dissipation Rates in the Cloudy Boundary Layer, Journal of the Atmospheric Sciences, 63, 1451–1466, https://doi.org/10.1175/JAS3687.1, https://doi.org/10.1175/JAS3687.1, 760 2006b.

SOMAG: GSM 4000 – Specifications, SOMAG AG Jena, https://www.somag-ag.de/fileadmin/user_upload/GSM_4000/Dokumente/112300_906_08_05_GSM_4000_Specifications.pdf, 2017.

Sreenivasan, K. R.: On the universality of the Kolmogorov constant, Physics of Fluids, 7, 2778–2784, https://doi.org/10.1063/1.868656, https://doi.org/10.1063/1.868656, 1995.

765 Stein, A. F., Draxler, R. R., Rolph, G. D., Stunder, B. J. B., Cohen, M. D., and Ngan, F.: NOAA's HYSPLIT Atmospheric Transport and Dispersion Modeling System, Bulletin of the American Meteorological Society, 96, 2059–2077, https://doi.org/10.1175/BAMS-D-14-00110.1, https://doi.org/10.1175/BAMS-D-14-00110.1, 2015.

Stephens, G. L., Vane, D. G., Tanelli, S., Im, E., Durden, S., Rokey, M., Reinke, D., Partain, P., Mace, G. G., Austin, R., L'Ecuyer, T., Haynes, J., Lebsock, M., Suzuki, K., Waliser, D., Wu, D., Kay, J., Gettelman, A., Wang, Z., and Marchand, R.: CloudSat mission: Performance and 770 early science after the first year of operation, Journal of Geophysical Research: Atmospheres, 113, https://doi.org/10.1029/2008JD009982, https://agupubs.onlinelibrary.wiley.com/doi/abs/10.1029/2008JD009982, 2008.

Tjernström, M., Leck, C., Persson, P. O. G., Jensen, M. L., Oncley, S. P., and Targino, A.: The Summertime Arctic Atmosphere: Meteorological Measurements during the Arctic Ocean Experiment 2001, Bulletin of the American Meteorological Society, 85, 1305–1322, https://doi.org/10.1175/BAMS-85-9-1305, https://doi.org/10.1175/BAMS-85-9-1305, 2004.

775 Tjernström, M., Shupe, M. D., Brooks, I. M., Persson, P. O. G., Prytherch, J., Salisbury, D. J., Sedlar, J., Achtert, P., Brooks, B. J., Johnston, P. E., Sotiropoulou, G., and Wolfe, D.: Warm-air advection, air mass transformation and fog causes rapid ice melt, Geophys. Res. Lett., 42, 5594–5602, https://doi.org/10.1002/2015gl064373, https://doi.org/10.1002/2015GL064373, 2015.

Tjernström, M., Leck, C., Birch, C. E., Bottenheim, J. W., Brooks, B. J., Brooks, I. M., Bäcklin, L., Chang, R. Y.-W., de Leeuw, G., Di Liberto, L., de la Rosa, S., Granath, E., Graus, M., Hansel, A., Heintzenberg, J., Held, A., Hind, A., Johnston, P., Knulst, J., Martin, M., Matrai, 780 P. A., Mauritsen, T., Müller, M., Norris, S. J., Orellana, M. V., Orsini, D. A., Paatero, J., Persson, P. O. G., Gao, Q., Rauschenberg, C., Ristovski, Z., Sedlar, J., Shupe, M. D., Sierau, B., Sirevaag, A., Sjogren, S., Stetzer, O., Swietlicki, E., Szczodrak, M., Vaattovaara, P., Wahlberg, N., Westberg, M., and Wheeler, C. R.: The Arctic Summer Cloud Ocean Study (ASCOS): overview and experimental design, Atmospheric Chemistry and Physics, 14, 2823–2869, https://doi.org/10.5194/acp-14-2823-2014, https://www.atmos-chem-phys.net/14/2823/2014/, 2014.

785 Uttal, T., Curry, J. A., McPhee, M. G., Perovich, D. K., Moritz, R. E., Maslanik, J. A., Guest, P. S., Stern, H. L., Moore, J. A., Turenne, R., Heiberg, A., Serreze, M. C., Wylie, D. P., Persson, O. G., Paulson, C. A., Halle, C., Morison, J. H., Wheeler, P. A., Makshtas, A., Welch, H., Shupe, M. D., Intrieri, J. M., Stamnes, K., Lindsey, R. W., Pinkel, R., Pegau, W. S., Stanton, T. P., and Grenfeld, T. C.: Surface Heat Budget of the Arctic Ocean, Bulletin of the American Meteorological Society, 83, 255–276, https://doi.org/10.1175/1520-0477(2002)083<0255:SHBOTA>2.3.CO;2, https://doi.org/10.1175/1520-0477(2002)083<0255:SHBOTA>2.3.CO;2, 2002.

790 Wendisch, M., Brückner, M., Burrows, J. P., Crewell, S., Dethloff, K., Ebell, K., Lüpkes, C., Macke, A., Notholt, J., Quaas, J., Rinke, A., and
      Tegen, I.: Understanding causes and effects of rapid warming in the Arctic, Eos, 98, https://doi.org/10.1029/2017EO064803, 2017.

Wendisch, M., Macke, A., Ehrlich, A., Lüpkes, C., Mech, M., Chechin, D., Dethloff, K., Velasco, C. B., Bozem, H., Brückner, M., Clemen,
      H.-C., Crewell, S., Donth, T., Dupuy, R., Ebell, K., Egerer, U., Engelmann, R., Engler, C., Eppers, O., Gehrmann, M., Gong, X.,
      Gottschalk, M., Gourbeyre, C., Griesche, H., Hartmann, J., Hartmann, M., Heinold, B., Herber, A., Herrmann, H., Heygster, G., Hoor, P.,
795 Jafariserajehlou, S., Jäkel, E., Järvinen, E., Jourdan, O., Kästner, U., Kecorius, S., Knudsen, E. M., Köllner, F., Kretzschmar, J., Lelli, L.,
      Leroy, D., Maturilli, M., Mei, L., Mertes, S., Mioche, G., Neuber, R., Nicolaus, M., Nomokonova, T., Notholt, J., Palm, M., van Pinx-
      teren, M., Quaas, J., Richter, P., Ruiz-Donoso, E., Schäfer, M., Schmieder, K., Schnaiter, M., Schneider, J., Schwarzenböck, A., Seifert, P.,
      Shupe, M. D., Siebert, H., Spreen, G., Stapf, J., Stratmann, F., Vogl, T., Welti, A., Wex, H., Wiedensohler, A., Zanatta, M., and Zeppenfeld,
      S.: The Arctic Cloud Puzzle: Using ACLOUD/PASCAL Multiplatform Observations to Unravel the Role of Clouds and Aerosol Particles
800 in Arctic Amplification, Bulletin of the American Meteorological Society, 100, 841–871, https://doi.org/10.1175/BAMS-D-18-0072.1,
      https://doi.org/10.1175/BAMS-D-18-0072.1, 2019.

Winker, D. M., Pelon, J. R., and McCormick, M. P.: CALIPSO mission: spaceborne lidar for observation of aerosols and clouds, in: Lidar
      Remote Sensing for Industry and Environment Monitoring III, edited by Singh, U. N., Itabe, T., and Liu, Z., vol. 4893, pp. 1 – 11,
      International Society for Optics and Photonics, SPIE, https://doi.org/10.1117/12.466539, https://doi.org/10.1117/12.466539, 2003.

805 Wulfmeyer, V. and Janjić, T.: Twenty-Four-Hour Observations of the Marine Boundary Layer Using Shipborne NOAA High-Resolution
      Doppler Lidar, Journal of Applied Meteorology, 44, 1723–1744, https://doi.org/10.1175/JAM2296.1, https://doi.org/10.1175/JAM2296.1,
      2005.

Yeo, H., Park, S.-J., Kim, B.-M., Shiobara, M., Kim, S.-W., Kwon, H., Kim, J.-H., Jeong, J.-H., Park, S. S., and Choi, T.: The observed
      relationship of cloud to surface longwave radiation and air temperature at Ny-Ålesund, Svalbard, Tellus B: Chemical and Physical Mete-
810 orology, 70, 1–10, https://doi.org/10.1080/16000889.2018.1450589, https://doi.org/10.1080/16000889.2018.1450589, 2018.

Young, G., Jones, H. M., Choularton, T. W., Crosier, J., Bower, K. N., Gallagher, M. W., Davies, R. S., Renfrew, I. A., Elvidge, A. D.,
      Darbyshire, E., Marenco, F., Brown, P. R. A., Ricketts, H. M. A., Connolly, P. J., Lloyd, G., Williams, P. I., Allan, J. D., Taylor, J. W.,
      Liu, D., and Flynn, M. J.: Observed microphysical changes in Arctic mixed-phase clouds when transitioning from sea ice to open ocean,
      Atmospheric Chemistry and Physics, 16, 13 945–13 967, https://doi.org/10.5194/acp-16-13945-2016, https://www.atmos-chem-phys.net/
815 16/13945/2016/, 2016.

Zhang, D., Wang, Z., Heymsfield, A., Fan, J., and Luo, T.: Ice Concentration Retrieval in Stratiform Mixed-Phase Clouds Using Cloud
      Radar Reflectivity Measurements and 1D Ice Growth Model Simulations, Journal of the Atmospheric Sciences, 71, 3613–3635,
      https://doi.org/10.1175/JAS-D-13-0354.1, https://doi.org/10.1175/JAS-D-13-0354.1, 2014.

Zhou, M. Y., Lenschow, D. H., Stankov, B. B., Kaimal, J. C., and Gaynor, J. E.: Wave and Turbulence Structure in a Shallow Baroclinic
820 Convective Boundary Layer and Overlying Inversion, Journal of the Atmospheric Sciences, 42, 47–57, https://doi.org/10.1175/1520-
      0469(1985)042<0047:WATSIA>2.0.CO;2, https://doi.org/10.1175/1520-0469(1985)042<0047:WATSIA>2.0.CO;2, 1985.